HOKKAIDO UNIVERSITY

Title	Interstation phase speed and amplitude measurements of surface waves with nonlinear waveform fitting : application to USArray
Author(s)	Hamada, K.; Yoshizawa, K.
Citation	Geophysical journal international, 202(3), 1463-1482 https://doi.org/10.1093/gji/ggv213
Issue Date	2015-09
Doc URL	http://hdl.handle.net/2115/60080
Type	article
File Information	1463.full.pdf

Instructions for use

Hokkaido University Collection of Scholarly and Academic Papers : HUSCAP

Geophysical Journal International

Geophys. J. Int. (2015) **202,** 1463–1482 doi: 10.1093/gji/ggv213
GJI Seismology

Interstation phase speed and amplitude measurements of surface waves with nonlinear waveform fitting: application to USArray

K. Hamada[1] and K. Yoshizawa[2]

[1] *Department of Natural History Sciences, Graduate School of Science, Hokkaido University, Sapporo* 060-0810, *Japan. E-mail: kouta@mail.sci.hokudai.ac.jp*
[2] *Department of Earth and Planetary Sciences, Faculty of Science, Hokkaido University, Sapporo* 060-0810, *Japan*

Accepted 2015 May 20. Received 2015 May 12; in original form 2014 May 13

SUMMARY

A new method of fully nonlinear waveform fitting to measure interstation phase speeds and amplitude ratios is developed and applied to USArray. The Neighbourhood Algorithm is used as a global optimizer, which efficiently searches for model parameters that fit two observed waveforms on a common great-circle path by modulating the phase and amplitude terms of the fundamental-mode surface waves. We introduce the reliability parameter that represents how well the waveforms at two stations can be fitted in a time–frequency domain, which is used as a data selection criterion. The method is applied to observed waveforms of USArray for seismic events in the period from 2007 to 2010 with moment magnitude greater than 6.0. We collect a large number of phase speed data (about 75 000 for Rayleigh and 20 000 for Love) and amplitude ratio data (about 15 000 for Rayleigh waves) in a period range from 30 to 130 s. The majority of the interstation distances of measured dispersion data is less than 1000 km, which is much shorter than the typical average path-length of the conventional single-station measurements for source-receiver pairs. The phase speed models for Rayleigh and Love waves show good correlations on large scales with the recent tomographic maps derived from different approaches for phase speed mapping; for example, significant slow anomalies in volcanic regions in the western Unites States and fast anomalies in the cratonic region. Local-scale phase speed anomalies corresponding to the major tectonic features in the western United States, such as Snake River Plains, Basin and Range, Colorado Plateau and Rio Grande Rift have also been identified clearly in the phase speed models. The short-path information derived from our interstation measurements helps to increase the achievable horizontal resolution. We have also performed joint inversions for phase speed maps using the measured phase and amplitude ratio data of vertical component Rayleigh waves. These maps exhibit better recovery of phase speed perturbations, particularly where the strong lateral velocity gradient exists in which the effects of elastic focussing can be significant; that is, the Yellowstone hotspot, Snake River Plains, and Rio Grande Rift. The enhanced resolution of the phase speed models derived from the interstation phase and amplitude measurements will be of use for the better seismological constraint on the lithospheric structure, in combination with dense broad-band seismic arrays.

Key words: Inverse theory; Surface waves and free oscillations; Seismic tomography; North America.

1 INTRODUCTION

The structure and dynamics of the upper mantle are closely related to the occurrence of earthquakes and volcanic activities near the surface of the Earth. Seismic surface waves provide us with a powerful means to map the lateral heterogeneity and anisotropy in the crust and upper mantle, and a number of tomographic studies using surface waves have been conducted in the past three decades on a variety of scales. Many of global surface wave studies have been based on the measurements of phase velocities between the source and receiver for the fundamental mode (e.g. Montagner & Tanimoto 1991; Trampert & Woodhouse 1995; Laske & Masters 1996; Ekström *et al.* 1997; Boschi *et al.* 2006). The majority of recent regional-scale tomography employs multimode waveform fitting techniques incorporating higher-mode information which helps in enhancing the depth resolution (e.g. van der Lee & Nolet 1997; Debayle & Kennett 2000; Lebedev & Nolet 2003; Isse *et al.* 2006b; Yoshizawa 2014), which have also been applied to the reconstruction of some recent global-scale models (e.g. Lebedev & van der Hilst 2008; Visser *et al.* 2008; Debayle & Ricard 2012). Such

© The Authors 2015. Published by Oxford University Press on behalf of The Royal Astronomical Society.

Downloaded from http://gji.oxfordjournals.org/ at Hokkaido University on October 20, 2015

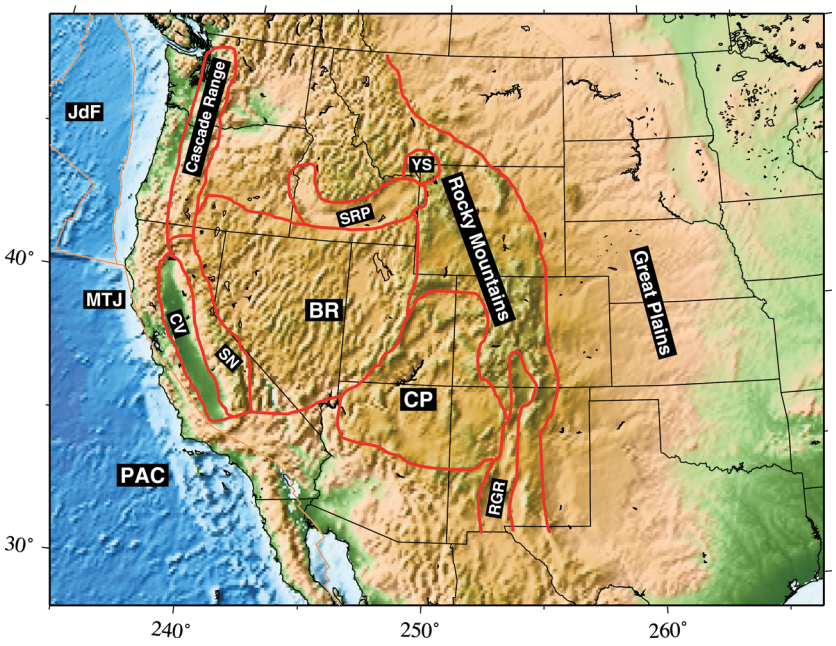

Figure 1. A topographic map of the western United States. Boundaries of tectonic provinces (red lines) are reproduced from Obrebski *et al.* (2011), and tectonic boundaries (orange lines) are taken from Bird (2003). YS: Yellowstone Caldera; SRP: Snake River Plain; RGR: Rio Grande Rift; CP: Colorado Plateau; BR: Basin and Range; SN: Sierra Nevada; GV: Great Valley; JdF: Juan de Fuca Plate; MTJ: Mendocino Triple Junction; PAC: Pacific Plate.

single-station techniques for surface-wave dispersion analysis generally require long propagation paths over 1000 km to assure the separation of surface-wave signals from the preceding body wave arrivals.

One of the widely used classical techniques in the regional-scale surface-wave mapping is the two-station method (e.g. Dziewonski & Hales 1972), in which the phase differences between seismograms at two stations on a common great-circle path are used to extract the average phase speed between two stations. By taking the phase difference between the two seismograms in the frequency domain, source terms can be cancelled out, so that no information on source mechanisms is needed in this style of technique. This method allows us to measure the phase speeds for short paths less than 1000 km between two stations, and can be useful for extending the resolution of velocity models in comparison with the single-station method.

There are many examples of the regional- or local-scale surface wave maps employing the interstation measurements of surface wave phase speeds; e.g. by employing permanent regional networks (e.g. Yoshizawa *et al.* 2010; Bakirci *et al.* 2012) and temporary deployments of broadband arrays (e.g. Isse *et al.* 2006a; Deschamps *et al.* 2008; Darbyshire & Lebedev 2009). Several studies have attempted to correct the deviation from the great circle by measuring the actual orientation of the wave front and calculating the velocities using the real interstation distance covered by the wave path (Baumont *et al.* 2002; Kaviani *et al.* 2007). Array style analysis for teleseismic tomography has also been investigated by modelling the arrival angles of incoming seismic waves and the phase velocity variations across the array simultaneously (e.g. Li *et al.* 2003).

A limitation of the two-station analysis is that two stations need to be located on or near the common great-circle path, which tends to restrict the available numbers of interstation dispersion measurements. This can be overcome by the use of dense broad-band seismic networks, which are becoming available in many regions over the world. USArray, deployed across the United States as a part of the Earthscope project, is one of the most prominent seismic networks for the application of interstation surface wave mapping.

The shear wave structure of North America, which encompasses complex tectonic features (Fig. 1), has been studied by using a variety of methods of surface wave analysis. The single-station method has been primarily used to constrain the large-scale *S*-wave structure (e.g. van der Lee & Nolet 1997; Godey *et al.* 2003; Marone *et al.* 2007; Nettles & Dziewonski 2008), employing permanent global networks and local stations in the United States. The deployment of the Transportable Array (TA; USArray) in the last decade provides us with high-quality broad-band seismic waveform data, which have facilitated a variety of tomographic studies in this region; for example, ambient noise tomography (e.g. Shapiro *et al.* 2005; Ekström *et al.* 2009), body-wave tomography (e.g. Burdick *et al.* 2010), higher-mode phase speed mapping of surface waves (Yoshizawa & Ekström 2010) and joint tomography of body and surface waves (Obrebski *et al.* 2011).

New multiple-station techniques for constraining seismic structure have also been developed for making the most of the USArray data; for example, eikonal tomography (Lin *et al.* 2009), Helmholtz tomography (Lin & Ritzwoller 2011) and two-station phase estimations based on single-station measurements with the arrival-angle corrections using a miniarray method (Foster *et al.* 2014b). The velocity models of these studies are consistent and the USArray data have dramatically enhanced horizontal resolution of tomographic models in the United States.

The majority of the two-station studies have used the phase information to constrain the velocity structure of the earth, and the use of the interstation amplitude information between two stations has been limited (e.g. Yang *et al.* 2004, for an attenuation study). The observed amplitude anomalies tend to be affected by a variety of effects, including focusing or defocusing effects caused by lateral heterogeneity of velocity structure, anelastic attenuation and scattering. The amplitude anomalies caused by focusing or defocusing effects depend on the second derivative of phase speed perpendicular to the ray path (e.g. Woodhouse & Wong 1986), and thus they are more sensitive to short-wavelength structure compared to the phase information. Thus, the amplitude information can be of help in

Downloaded from http://gji.oxfordjournals.org/ at Hokkaido University on October 20, 2015

improving lateral resolutions of phase speed models (e.g. Laske & Masters 1996; Yang & Forsyth 2006). While global-scale phase speed models using amplitude data for source-receiver paths have been investigated in detail by Dalton & Ekström (2006), local-scale phase speed models incorporating interstation amplitude ratios from a dense seismic array have yet to be investigated.

In this study, we develop a new approach for the surface wave phase speed and amplitude measurements between two stations on a common great-circle path, based on a fully nonlinear interstation waveform fitting technique working with the Neighbourhood Algorithm (NA; Sambridge 1999) as a global optimizer. In the recent study of two-station method using USArray by Foster *et al.* (2014b), the interstation phase information has been derived from the single-station phase measurements for each station, based on the work by Ekström *et al.* (1997). We, instead, employ the direct comparisons of waveforms at two stations to extract the interstation phase speeds and amplitude ratios simultaneously. The basic idea of this method of nonlinear waveform fitting is modelled in the earlier work by Yoshizawa & Kennett (2002) and Yoshizawa & Ekström (2010), in which a single station seismogram is inverted using NA to extract path-specific multimode phase speeds for source–receiver pairs. The new method of two-station waveform matching is applied to the large number of station pairs of USArray in an automated manner by employing quantitative evaluation criteria for the quality control of the estimated interstation phase speed and amplitude. The main emphasis of this study is placed on the development and application of the new technique of the interstation phase and amplitude measurements of the fundamental-mode surface waves working with a dense broad-band seismic array. The resultant phase speed models for both Love and Rayleigh waves will be discussed in comparison with recent tomographic studies in North America. We will also discuss phase speed models derived from the joint inversions of the phase and amplitude data for the vertical Rayleigh waves, which exhibits the importance of amplitude information to better constrain the smaller-scale heterogeneity across the array.

2 METHOD OF PHASE SPEED AND AMPLITUDE MEASUREMENTS

In this study, we develop a new method of fully nonlinear waveform fitting to extract interstation phase speeds. The Neighbourhood Algorithm (NA) of Sambridge (1999) is used as a global optimizer to find the best dispersion curve that matches two observed waveforms. We employ a reliability parameter that represents how well the waveforms at two stations can be fitted in a time–frequency domain, which is then used as a data selection criterion in the subsequent step of phase speed mapping. In this section, we summarize the formulations for the fully nonlinear waveform fitting to estimate interstation phase speeds and amplitude ratios.

2.1 Formulation for interstation waveform fitting

We define the seismogram of the nearer station in the frequency domain as $u^{\rm near}(\omega)$, and that of the farther station as $u^{\rm far}(\omega)$, which can be represented as

$$u^{\rm far}(\omega) = A^{\rm far}(\omega)\exp[i\phi^{\rm far}(\omega)], \tag{1}$$

$$u^{\rm near}(\omega) = A^{\rm near}(\omega)\exp[i\phi^{\rm near}(\omega)], \tag{2}$$

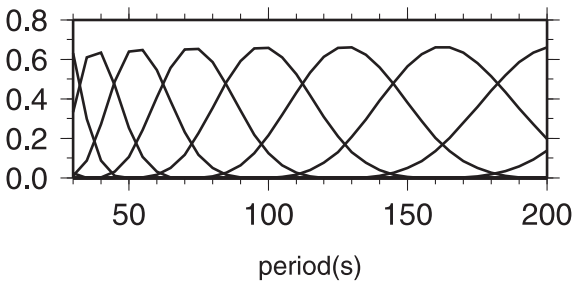

Figure 2. An example of a set of B-spline functions in a period range between 30 and 200 s.

where $\phi^{\rm far}$ and $\phi^{\rm near}$ are the phase terms, $A^{\rm far}$ and $A^{\rm near}$ are the amplitude terms corrected respectively with geometrical spreading factors $\sqrt{\sin\Delta^{far}}$ and $\sqrt{\sin\Delta^{near}}$, and $\Delta^{\rm far}$ and $\Delta^{\rm near}$ are the epicentral distances for each station. Now, we try to find the best estimate of a transfer function $T(\omega)$ between $u^{\rm far}$ and $u^{\rm near}$, which eventually gives us with the interstation phase and amplitude ratio as a function of frequency. Using the transfer function defined as $T(\omega) = D(\omega)\exp[i\delta\phi(\omega)]$, where D is the amplitude ratio and $\delta\phi$ the phase differences between the two stations, we can express the perturbed seismogram $u^{\rm pert}$ as follows,

$$\begin{aligned} u^{\rm pert}(\omega) &= T(\omega)u^{\rm near}(\omega) \\ &= A^{\rm near}(\omega)D(\omega)\exp\left[i\left\{\phi^{\rm near}(\omega)+\delta\phi(\omega)\right\}\right]. \end{aligned} \tag{3}$$

The amplitude ratio D and phase difference $\delta\phi$ can be explicitly given as follows,

$$D = \frac{A^{\rm far}}{A^{\rm near}} = D_0 + \delta D, \tag{4}$$

$$\delta\phi = -\frac{\omega d\Delta}{c_0+\delta c}, \tag{5}$$

where $d\Delta$ is the distance between two stations, $D_0(=\exp[-\omega d\Delta Q_0^{-1}/2U_0])$, U_0, c_0 and Q_0^{-1} are the reference values for amplitude ratio, group speed, phase speed and inverse quality factor for a reference model. In this study, a modified version of PREM (Preliminary Reference Earth Model; Dziewonski & Anderson 1981), in which the 220 km discontinuity is smoothed out, is used as the reference model.

To estimate the optimum dispersion curves by fitting two seismograms $u^{\rm far}$ and $u^{\rm pert}$, the fractional perturbations of path-specific phase speed δc and amplitude ratio δD are expanded in a set of B-spline functions $f_i(\omega)$,

$$\delta c = \sum_{i=1}^{N} b_i f_i(\omega), \tag{6}$$

$$\delta D = \sum_{i=1}^{N} d_i f_i(\omega), \tag{7}$$

where N is the number of parameters and B-spline functions. The coefficients b_i and d_i for the ith B-spline are the model parameters to be determined through the nonlinear waveform fitting. An example of a set of B-splines as a function of period is shown in Fig. 2. In this study, after several trials, we decided to use nine B-spline functions (i.e. $N = 9$) to represent the smoothly varying perturbation of dispersion curves in the period range from 30 to 200 s. We adopt the NA by Sambridge (1999) as a global optimizer that effectively searches for sets of model parameters with smaller misfit. We set the

Downloaded from http://gji.oxfordjournals.org/ at Hokkaido University on October 20, 2015

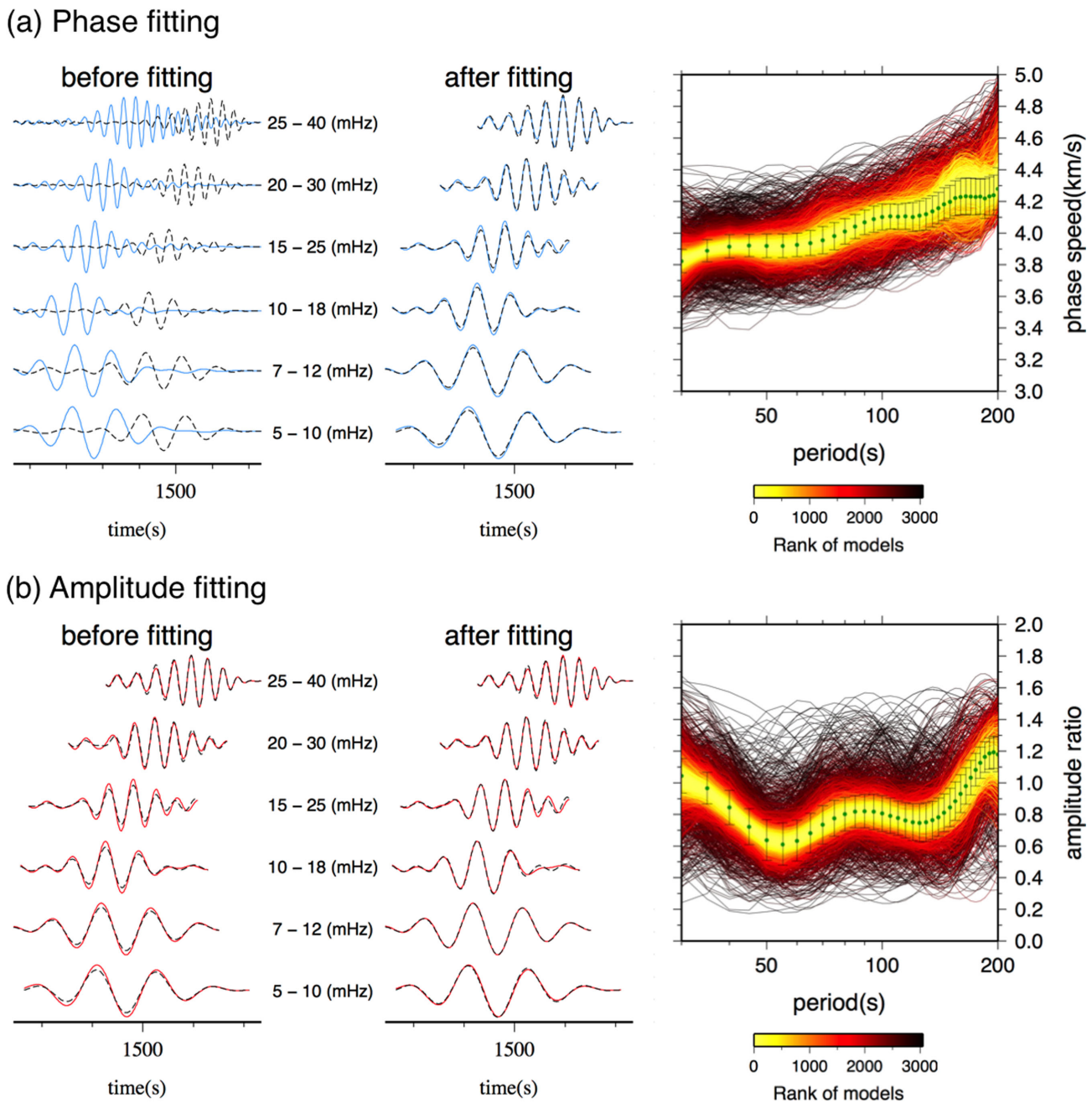

Figure 3. Examples of waveform fitting for the fundamental-mode Rayleigh waves, showing six time windows with different frequency ranges, for a station pair L20A (u^{near}) and P13A (u^{far}) from a seismic event in Samoa at 10 km depth on 2007 December 13. (a) Before and after the waveform fitting by perturbing the phase speed term only (no amplitude fitting), and the resultant phase speed dispersion curves (on the right), derived from the phase-term fitting through the NA. All the 3050 models exploited by the NA are ranked in order of the smaller misfit, and are plotted with colours varying from dark brown (larger misfit) to yellow (smaller misfit). The green dots represent the best-fit dispersion measurements with error bars calculate from the ensemble of all dispersion curves. (b) Before and after the waveform fitting by perturbing the amplitude term, and measured amplitude ratios.

parameter search range with NA such that ± 0.6 km s^{-1} for phase speed coefficients b_i , and ± 0.8 for amplitude ratios coefficients d_i. The details of nonlinear waveform fitting with NA will be explained in Section 2.2.

The waveform fitting process of this study takes two steps. First, we perturb only the phase term of u^{near} to fit the seismogram at a farther station. This will enable us to determine interstation dispersion curves of phase speeds. The measurement reliability (see Section 2.3) for the phase speeds is evaluated using the fitted waveforms whose amplitudes are normalized. In the second step, we compute perturbed waveforms by modulating the amplitude term to further fit u^{pert} to u^{far}, and evaluate the reliability for the estimated amplitude ratios using the total waveform fit. The reliability parameter employed in this study will be fully described in Section 2.3. The procedure of our nonlinear waveform fitting is summarized visually in Fig. 3.

Downloaded from http://gji.oxfordjournals.org/ at Hokkaido University on October 20, 2015

Table 1. A summary of time window setting for the fundamental-mode Rayleigh and Love waves used in this study. $\hat{U}$ is the reference group speed for Rayleigh/Love waves evaluated at the middle of each frequency band, calculated from the global group speed model (Larson & Ekström 2001) for each path.

Frequency range (mHz)	Min (km s^{-1})	Max (km s^{-1})
5–10	$\hat{U} - 0.42$	$\hat{U} + 0.52$
7–12	$\hat{U} - 0.40$	$\hat{U} + 0.50$
10–18	$\hat{U} - 0.36$	$\hat{U} + 0.46$
15–25	$\hat{U} - 0.32$	$\hat{U} + 0.42$
20–30	$\hat{U} - 0.27$	$\hat{U} + 0.37$
25–40	$\hat{U} - 0.24$	$\hat{U} + 0.34$

2.2 Global optimization with Neighbourhood Algorithm

The NA (Sambridge 1999) is a global search method for finding models with acceptable data fit in a multidimensional parameter space. This algorithm makes use of the natural neighbours, known as Voronoi cells, to implement the parameter search, and requires only two tuning parameters. The basic procedure of NA is summarized as follows:

(1) Generate an initial set of n_s models uniformly in the parameter space.
(2) Calculate the misfit function for the most recently generated set of n_s models and determine the n_r models with the lowest misfit of all models generated so far.
(3) Generate n_s new models by performing a uniform random walk in the Voronoi cell for each of the n_r chosen models.
(4) Repeat (2) and (3).

In this study, we generate 50 initial models first, and then the model parameter search using the NA is iterated for 300 times with $n_s = 10$ and $n_r = 5$, so that 3050 models are generated in total for each pair of seismograms.

To evaluate the misfit between the two waveforms $u^{\mathrm{far}}(t)$ and $u^{\mathrm{pert}}(t) = T(t) * u^{\mathrm{near}}(t)$ in the time domain (where the asterisk represents convolution), we use a misfit function which is defined as,

$$\Phi = \sum_{i=1}^{n_f} \{F_i u^{\mathrm{far}}(t) - F_i u^{\mathrm{pert}}(t)\}^2, \tag{8}$$

where F_i represents ith bandpass filter ($i = 1, \ldots, n_f$), and n_f is the number of bandpass filters with different frequency ranges. We employ six bandpass filters to achieve the best waveform fit in a wide frequency range. Prior to the band-pass filtering, time windows are automatically determined by taking account of the path-average group speeds for each path and frequency, which are estimated from global group speed maps by Larson & Ekström (2001), so that the fundamental-mode Love and Rayleigh waves are properly included in the chosen window. The time window setting and frequency ranges for bandpass filters used in this study are summarized in Table 1.

One of the critical issues in the interstation phase measurements is $2n\pi$ ambiguity in the phase term (where n is an arbitrary integer), which may results in the phase cycle skip. Our smoothed parameterization of dispersion curves using the B-spline functions as well as the waveform matching with multiple bandpass filters including two long-period filters over 100 s can be of help to reduce the occurrence of phase skip during the waveform fitting. Also in our global optimization method, the parameter search range for phase speed perturbation is limited within $\pm$ 0.6 km s^{-1} from the reference dispersion curve for PREM, which is much less than the expected velocity perturbations caused by $\pm 2\pi$ phase shift in the long period. Thus, our measurements are unlikely to be severely affected by the phase cycle skip, except for the period range shorter than 50 s with interstation distances longer than 2000 km, though the number of such data is very limited.

An example of Rayleigh waves before and after nonlinear fitting process is displayed in Fig. 3. We can see that the observed waveforms at the far station can be matched fairly well in a wide frequency range. In Fig. 3, we also show an example of a set of 3050 dispersion curves for phase speed and amplitude ratio as a function of period, which is derived from the nonlinear waveform fitting with NA. Yellow lines in the background indicate the models with smaller misfit, and the best-fit dispersion curve is shown with the green dots with error bars estimated from the ensemble of all dispersion curves. Note that such rough estimates of measurement errors depend on the convergence rate in the global optimization process, and it does not necessarily reflect meaningful errors in the dispersion measurements. Thus, in the next section, we consider the reliability parameter that quantifies how well the perturbed waveform is fitted with the reference waveform.

2.3 Reliability of dispersion measurements

As an efficient way to estimate the quality of measurements, we use the reliability parameter for the quantitative evaluation of the results of waveform fitting. The idea of the reliability for waveform fitting is modelled on the early works for multimode dispersion measurements for a source–receiver paths by van Heijst & Woodhouse (1997) and its modified versions by Yoshizawa & Kennett (2002) and Yoshizawa & Ekström (2010). Here, we briefly summarize the idea of how to quantify the goodness of the waveform fit and to estimate the frequency-dependent reliability of dispersion measurements.

First, we consider a residual seismogram $u^{\mathrm{res}}(t) = u^{\mathrm{far}}(t) - u^{\mathrm{pert}}(t)$. Then, we calculate the corresponding spectrograms $S^{\mathrm{res}}(\omega, t)$ and $S^{\mathrm{far}}(\omega, t)$ in the frequency–time domain. We define a waveform fit parameter $f(\omega, t)$, which quantifies how well the synthetic waveform u^{pert} is fitted with u^{far}, as follows:

$$f(\omega, t) = \exp\left[-\frac{S^{\mathrm{res}}(\omega, t)}{S^{\mathrm{far}}(\omega, t)}\right]. \tag{9}$$

The reliability parameter $r(\omega)$ as a function of ω is then calculated by integrating $f(\omega, t)$ by time and normalizing the result by its time window T_w,

$$r(\omega) = \frac{1}{T_w} \int_0^{T_w} f(\omega, t) \mathrm{d}t. \tag{10}$$

While the waveform misfit Φ in eq. (8) represents the degree of misfit between the two seismograms as a whole, the reliability parameter provides us with the frequency-dependent accuracy of estimated phase speed and amplitude ratio. Fig. 4 displays examples of the parameters $f(\omega, t)$ and $r(\omega)$, which vary from 0 (unreliable, mismatched waveforms) to 1 (reliable, perfect waveform fit).

Although the reliability parameter is basically an independent parameter from a measurement error, it can also be affected by the similar error sources in the measurements, such as the effects

Downloaded from http://gji.oxfordjournals.org/ at Hokkaido University on October 20, 2015

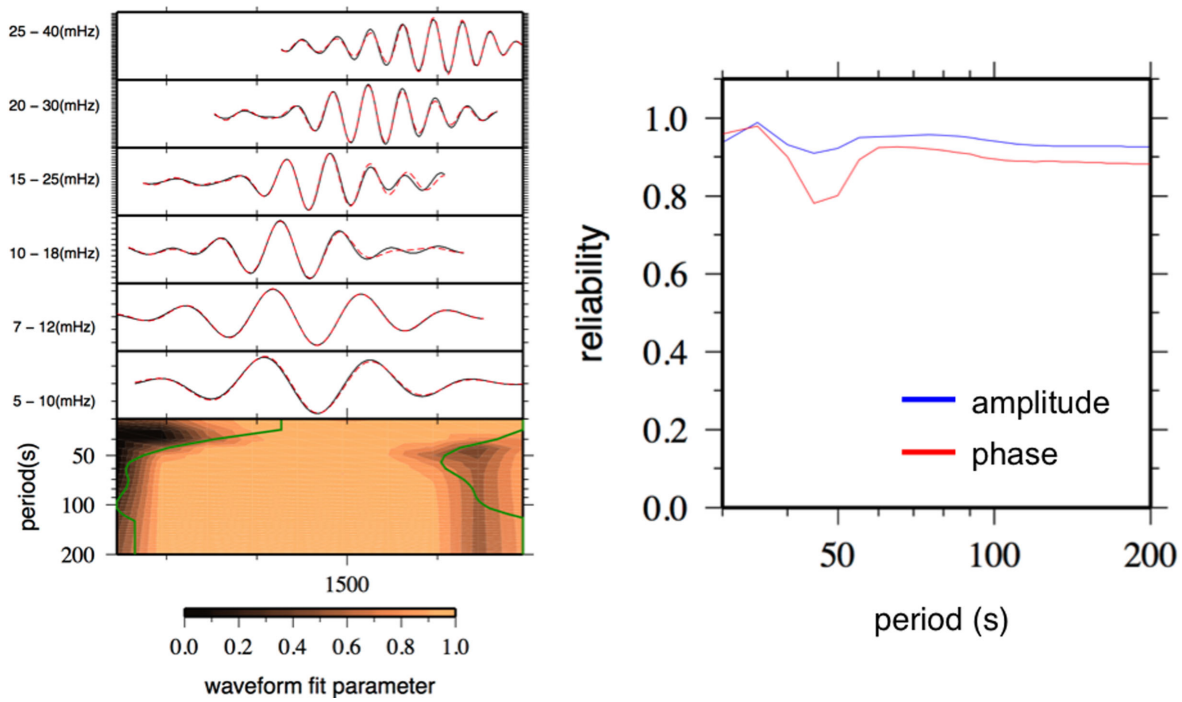

Figure 4. Left: (top) a perturbed waveform (red dashed line) and an observed waveform for the farther station from the source (black line) used in Fig. 3; (bottom) the waveform fit parameter $f(\omega, t)$ in the frequency–time domain. Green lines are the start and end time of the time window used for the waveform fitting. Right: reliability parameters $r(\omega)$ as a function of period, calculated from the matched waveforms with phase fitting (red line) and with amplitude fitting (blue line).

of off-great-circle propagation and the interferences of non-plane waves and/or higher modes, which may deteriorate the quality of waveform fitting under the assumption of our analysis; that is, a single plane-wave propagation along the great-circle path. We use the reliability parameter as an automatic data selection criterion and a weighting factor in the subsequent process of phase speed mapping in Section 4.

3 APPLICATION TO TRANSPORTABLE ARRAY

3.1 Events and stations

The interstation waveform fitting technique described in the previous section is applied to three-component waveforms observed at the TA stations of USArray and the Southern California Seismic Network (CI) stations. We have used seismic events occurred in the period between 2007 January and 2010 December with moment magnitudes 6.0 or greater. Fig. 5 shows the distributions of the events and stations used in this study. The USArray stations migrate gradually from west to east, and, by the end of 2010, it covers the western-half of the United States.

3.2 Waveform processing

The main target of our waveform analysis is to extract the interstation phase speeds and amplitude ratios of the fundamental-mode Rayleigh and Love waves in the period range between 30 and 200 s. Prior to the waveform fitting, the instrument response of each seismogram is deconvolved, and then all seismograms are convolved with the response function of STS-1 seismometer. Surface waves in the horizontal components (particularly, Love waves in this study) are likely to be affected by the misorientation of seismometers (e.g. Laske & Masters 1996; Yoshizawa *et al.* 1999). We therefore use the polarization anomalies estimated and provided by Ekström (http://www.ldeo.columbia.edu/~ekstrom/Projects/USARRAY/QC_2010/index.html) to correct the plausible misorientation of horizontal components at each station, when we rotate the horizontal components to the great-circle directions.

We also evaluate the radiation patterns of each event using the Global CMT solutions (Ekström *et al.* 2005) to minimize the large uncertainties in the phase speed measurements in the nodal direction of surface wave radiation. In this study, we have eliminated stations located in the near nodal direction in which the radiated amplitude is less than 50 per cent of the maximum surface-wave radiation.

The interstation waveform fitting method requires that two stations are located nearly on a common great-circle path. We select station pairs that satisfy the following conditions (Fig. 6); the difference in azimuths from a source to the two stations, α, is less than 0.5°, and the difference in back-azimuths, β, is less than 2.5°. We then perform the waveform fitting described in Section 2.2 and extract the dispersion curves of phase speeds and amplitude ratios between the two stations. The frequency-dependent reliability parameters in Section 2.3 are used as a guide to determine the frequency range with satisfactory accuracy for each dispersion curve.

With several empirical experiments, we use the threshold (or minimum) values of the reliability parameter r_c for the automatic selection of high-quality phase speed measurements as a function of period T, which is given as, $r_c(T) = r_0 \times \bar{r}(T)/\bar{r}(T_0)$, where T_0 is the reference period and $\bar{r}$ is the average reliability value for each period. In this study, we used a reference period of $T_0 = 80$ s, and $\bar{r}(T_0) = 0.6$ for Rayleigh waves and 0.7 for Love waves. The threshold values of the reliability parameter for the amplitude ratios are fixed to 0.9 at all the period.

Downloaded from http://gji.oxfordjournals.org/ at Hokkaido University on October 20, 2015

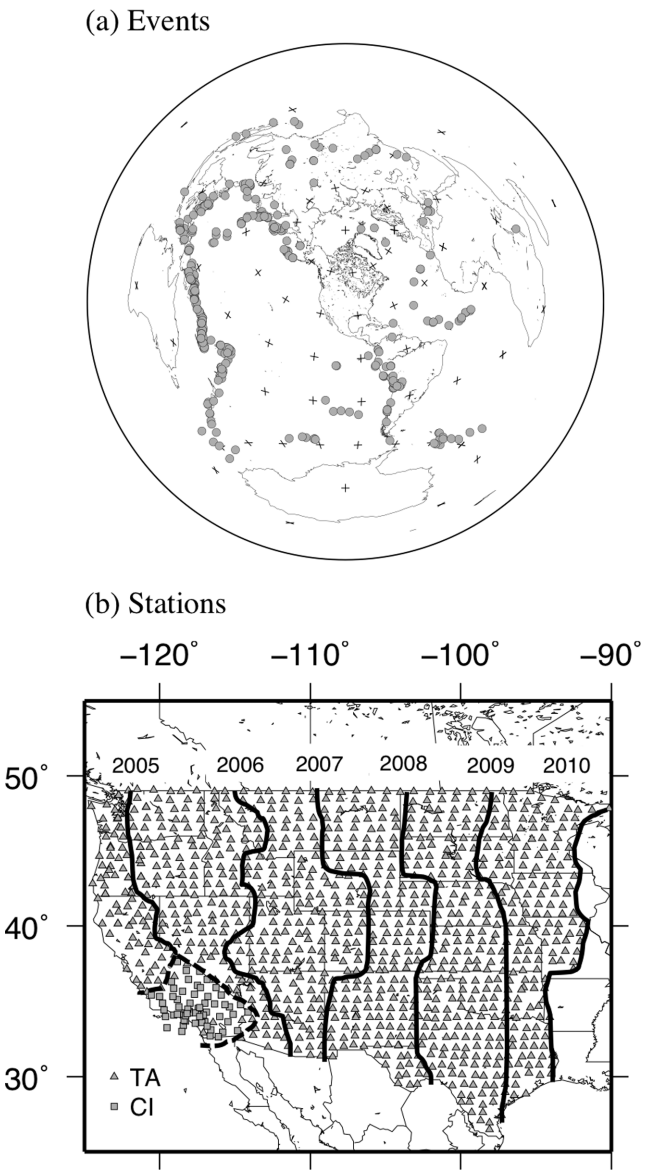

Figure 5. Distributions of (a) seismic events and (b) seismic stations used in this study. Transportable stations installed in the period from 2005 to 2010 are used. Black lines show the eastern edges of Transportable Array (TA) stations by the end of each year. A dashed line indicates the area of California Seismic Network (CI).

3.3 Data sets for phase speed and amplitude ratio

The numbers of measurements of phase speeds, which have successfully passed all of the required selection criteria, are summarized in Tables 2 and 3. We have gathered more than 50 000 station pairs for the Rayleigh waves and over 15 000 for Love waves in the majority of our target period range. The numbers of amplitude data for the vertical component Rayleigh waves have been collected for about 15 000 station pairs. The phase and amplitude measurements for Love waves tend to be noisier than those for Rayleigh waves, mainly due to lower signal-to-noise ratios in the horizontal components and higher-mode interference with the fundamental mode. Also, the number of amplitude measurements for Love waves are rather limited. Thus, in this study, we avoid to use the amplitude measurements for Love waves in the phase speed mapping explained in Section 4.

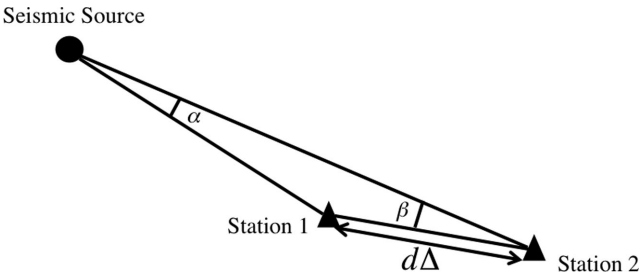

Figure 6. A geometrical configuration of two stations and a seismic source.

Fig. 7 displays the path density maps and the histogram of number of measurements as a function of interstation distance for Rayleigh-wave phase and amplitude and Love-wave phase at 80 s. The path density tends to be higher in the western areas than in the central areas (the eastern margin of our analysis), which represents the differences in the duration of observation period of the TA. The histograms of our measurements indicate that we have collected a large number of interstation surface wave dispersion data for short distances less than 1000 km. Such short-path information cannot readily be extracted from the conventional single-station analysis for surface waves and can be of great help in enhancing the horizontal resolution of phase speed models in North America.

Fig. 8 displays some typical examples of dispersion curves of both phase speed and amplitude ratios of Rayleigh waves for two station pairs; D13A and G05A stations, and FUR and MPP stations. The phase speed measurements for a longer path (Fig. 8b) exhibit fairly consistent values in a wider period range up to about 150 s with somewhat larger deviations in the longer period, while those for a shorter path (Fig. 8c) tend to be more scattered in the period longer than 100 s, for which the wavelength of Rayleigh waves becomes much larger than the interstation distance. The amplitude ratios between two stations tend to be more scattered compared to phase speeds, which results in somewhat lower variance reductions for the amplitude data in the joint inversions discussed later in Section 4.2. We have assumed a single plane wave propagation for the waveform fitting process, but this assumption may be violated if the effects of non-plane waves or off-great-circle signals are non-negligible (e.g. Pedersen 2006). Some outlying measurements pass the quality control requirements and are included in the large data sets extracted from our automated measurements. However, the majority of the measurements well reflect the average local features for each path, and the number of outliers is rather limited compared to our very large data set. The measured phase speeds in the longer periods tend to be unstable, particularly in case that the wavelength of surface waves becomes much longer than the interstation distances, which results in large measurement errors. Since the majority of our measured data sets comprises interstation distances shorter than 600 km, we avoid to use the measured phase speeds in the period longer than 130 s in the subsequent discussion of this paper.

4 MAPPING PHASE SPEED MODELS

We use the method of tomographic inversion of surface waves developed by Yoshizawa & Kennett (2004) to invert the interstation dispersion data for phase speed maps as a function of period. In this section, we briefly summarize the method of phase speed mapping using the observed phase and amplitude data, and display the phase speed maps in the western United States.

Downloaded from http://gji.oxfordjournals.org/ at Hokkaido University on October 20, 2015

Table 2. The numbers of measurements, station pairs, standard deviations σ_c and σ_A for the measured phase speed and amplitude ratios, and the threshold of reliability parameters r_c and r_A for phase speed and amplitude ratios, as a function of period for Rayleigh waves.

Period (s)	Rayleigh wave Measurements Phase	Measurements Amplitude	Station pairs Phase	Station pairs Amplitude	Standard deviation σ_c	Standard deviation σ_A	Threshold r_c	Threshold r_A
30	71 957	10 979	46 276	8632	0.120	0.305	0.555	0.900
40	75 452	12 806	50 386	11 410	0.123	0.353	0.567	0.900
50	75 510	7912	51 159	7101	0.127	0.255	0.555	0.900
60	76 731	11 174	52 090	9475	0.125	0.197	0.572	0.900
70	77 769	14 497	52 938	11 657	0.133	0.190	0.588	0.900
80	78 089	17 482	53 321	13 731	0.132	0.174	0.600	0.900
100	77 771	19 933	53 400	15 297	0.147	0.162	0.613	0.900
130	71 319	24 031	49 743	19 813	0.175	0.163	0.630	0.900

Table 3. Same as Table 2, but for the phase data of Love waves.

Period (s)	Love wave Measurements	Station pairs	σ_c	Threshold: r_c
30	21 988	16 742	0.146	0.741
40	20 969	16 813	0.142	0.800
50	22 029	17 597	0.169	0.756
60	23 890	19 129	0.184	0.732
70	24 623	19 744	0.206	0.710
80	25 073	20 310	0.220	0.700
100	22 886	19 276	0.241	0.694
130	15 635	13 955	0.283	0.714

4.1 Formulation of inversion for phase speed maps

4.1.1 Phase speed inversions using phase data

The observed path-average phase speeds between two stations can be expressed as follows,

$$\frac{\delta c^{\rm obs}}{c_0} = \frac{1}{d\Delta}\int_{g.c.} \frac{\delta c(s)}{c_0} {\rm d}s, \tag{11}$$

where $\frac{\delta c^{\rm obs}}{c_0} = \frac{c^{\rm obs}-c_0}{c_0}$, $c^{\rm obs}$ is the measured phase speed along the interstation path, c_0 the reference phase speed (i.e. in this study, we used average phase speed for all measurements) and the integration is taken along the great circle. Using eq. (11), frequency-dependent phase speed maps are constructed based on tomographic inversions with the assumption of surface wave propagation along the great-circle path.

The linearized equation (11) can be written in a generalized form,

$$\mathbf{d} = \mathbf{Gm}, \tag{12}$$

where $\mathbf{d}$ is the data vector that consists of the observed phase speed perturbation $d_i = (\delta c^{\rm obs}/c_0)_i (i = 1, 2, \ldots, M)$ and M is the total number of measurements. $\mathbf{G}$ is the kernel matrix and $\mathbf{m}$ is the model-parameter vector $m_j (j = 1, 2, \ldots, N)$, where N is the total number of model parameters to be determined through inversions.

A local phase speed perturbation can be expanded in spherical B-spline functions $B_j(\theta, \phi)$,

$$\frac{\delta c(\theta,\phi)}{c_0} = \sum_{j=1}^{N} m_j B_j(\theta,\phi), \tag{13}$$

where θ and ϕ are latitude and longitude, respectively, and the model parameter m_j is the coefficient for the jth basis function B_j. In this study, we use the constant grid interval of $1.0^\circ \times 1.0^\circ$ when we invert for the phase speed maps. Using the spherical B-spline functions, the components of the kernel matrix $\mathbf{G}$ for the ith measurement and the jth model parameter can be written as

$$G_{ij} = \frac{1}{d\Delta}\int_0^{d\Delta} B_j {\rm d}s. \tag{14}$$

The linearized equation (12) can be solved with a damped least-squares scheme, minimizing the following objective function,

$$\Phi(\mathbf{m}) = |\mathbf{d}' - \mathbf{G}'\mathbf{m}|^2 + \lambda^2 |\mathbf{m}|^2, \tag{15}$$

where the components of $\mathbf{d}'$ and $\mathbf{G}'$ are respectively $d_i' = (w_i/\sigma_c)d_i$ and $G_{ij}' = (w_i/\sigma_c)G_{ij}$, σ_c is the standard deviation of phase speed data for each period, and w_i is the weighting factor for the ith measurement for which we use the reliability parameter for each measurement (i.e. $w_i = r(\omega)$). λ is an arbitrary damping parameter which controls the trade-off between the data misfit $|\mathbf{d}' - \mathbf{G}'\mathbf{m}|^2$ and the model norm $|\mathbf{m}|^2$. We use the LSQR algorithm (Paige & Saunders 1982) to solve the linear inverse problem iteratively.

4.1.2 Phase speed inversions using interstation amplitude ratios

Observed amplitudes of surface waves include a variety of effects. The amplitude A at a single station, after the corrections for the geometrical spreading and the instrument response, can be represented as $A(\omega) = A_S(\omega) A_R(\omega) A_F(\omega) A_Q(\omega)$, where A_S represents the source term including radiation pattern and source excitation, A_R the receiver term including site amplification effects, A_F the elastic focusing/defocusing term and A_Q the anelastic attenuation term.

Now, we consider the amplitudes for both the farther and nearer stations to the source as follows, omitting the frequency dependency,

$$A^{\rm far} = A_S^{\rm far} A_R^{\rm far} A_F^{\rm far} A_Q^{\rm far}, \tag{16}$$

$$A^{\rm near} = A_S^{\rm near} A_R^{\rm near} A_F^{\rm near} A_Q^{\rm near}. \tag{17}$$

Considering that the source terms can be cancelled out in our two-station measurements along the great-circle paths (i.e. $A_S^{\rm far} = A_S^{\rm near}$), dividing eq. (16) by eq. (17) leads to the following relation,

$$\frac{A^{\rm far}}{A^{\rm near}} = \frac{A_R^{\rm far}}{A_R^{\rm near}} \frac{A_F^{\rm far}}{A_F^{\rm near}} \frac{A_Q^{\rm far}}{A_Q^{\rm near}}. \tag{18}$$

Downloaded from http://gji.oxfordjournals.org/ at Hokkaido University on October 20, 2015

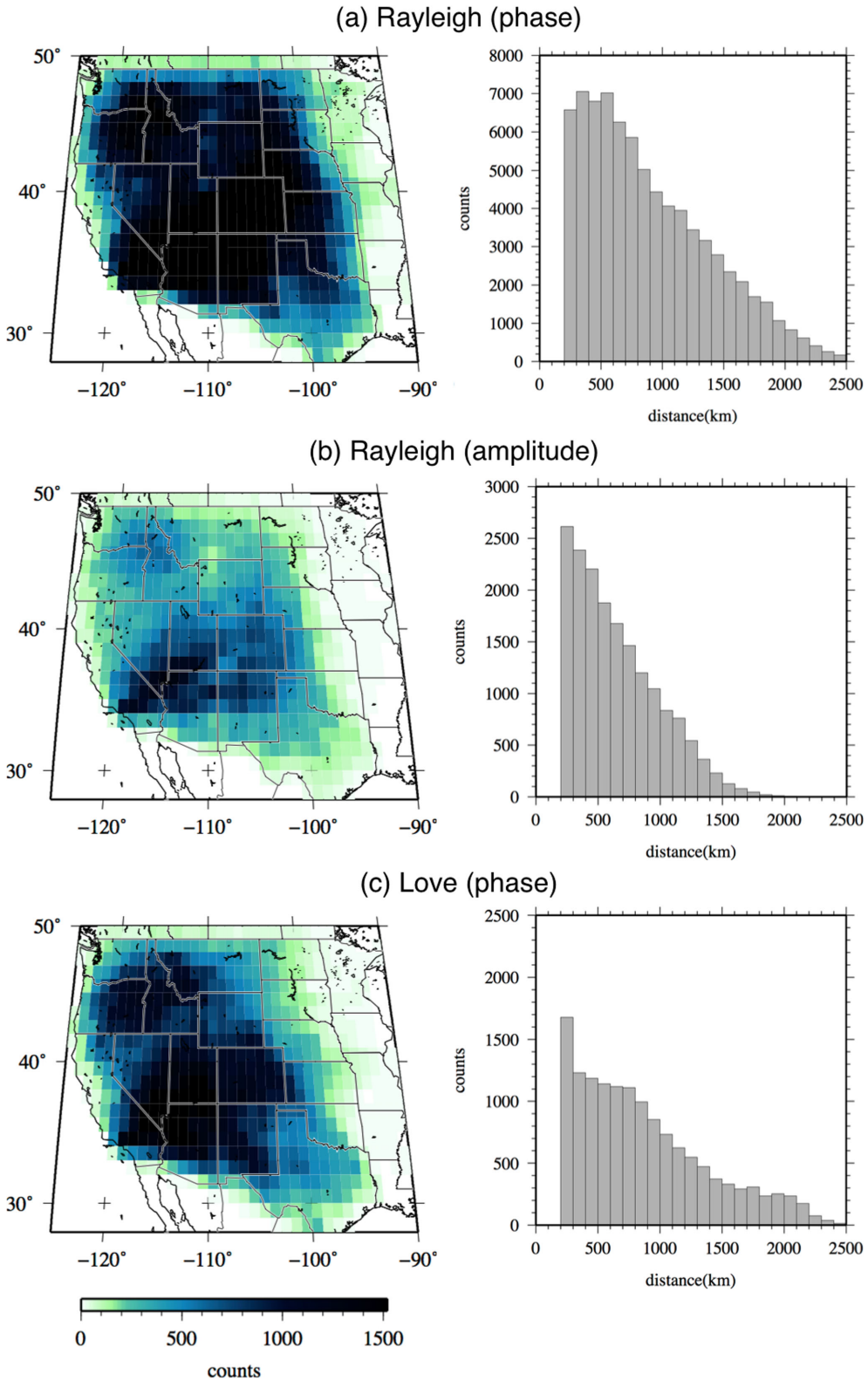

Figure 7. Left: the number of ray paths in 1° × 1° cells for (a) phase measurements and (b) amplitude measurements of Rayleigh waves at 80 s, and (c) the phase measurements of Love waves at 80s. Right: numbers of measurements for each data set as a function of interstation distances.

Taking the logarithm of both terms of eq. (18) yields,

$$\ln \frac{A^{\text{far}}}{A^{\text{near}}} = \ln A_R^{\text{far}} - \ln A_R^{\text{near}} + \ln \frac{A_F^{\text{far}}}{A_F^{\text{near}}} + \ln \frac{A_Q^{\text{far}}}{A_Q^{\text{near}}}. \tag{19}$$

The third term on the right-hand side represents the amplitude anomaly between the two stations caused by the effects of elastic focusing/defocusing due to the lateral heterogeneity of velocity structure. Following the linear perturbation theory by Woodhouse

Downloaded from http://gji.oxfordjournals.org/ at Hokkaido University on October 20, 2015

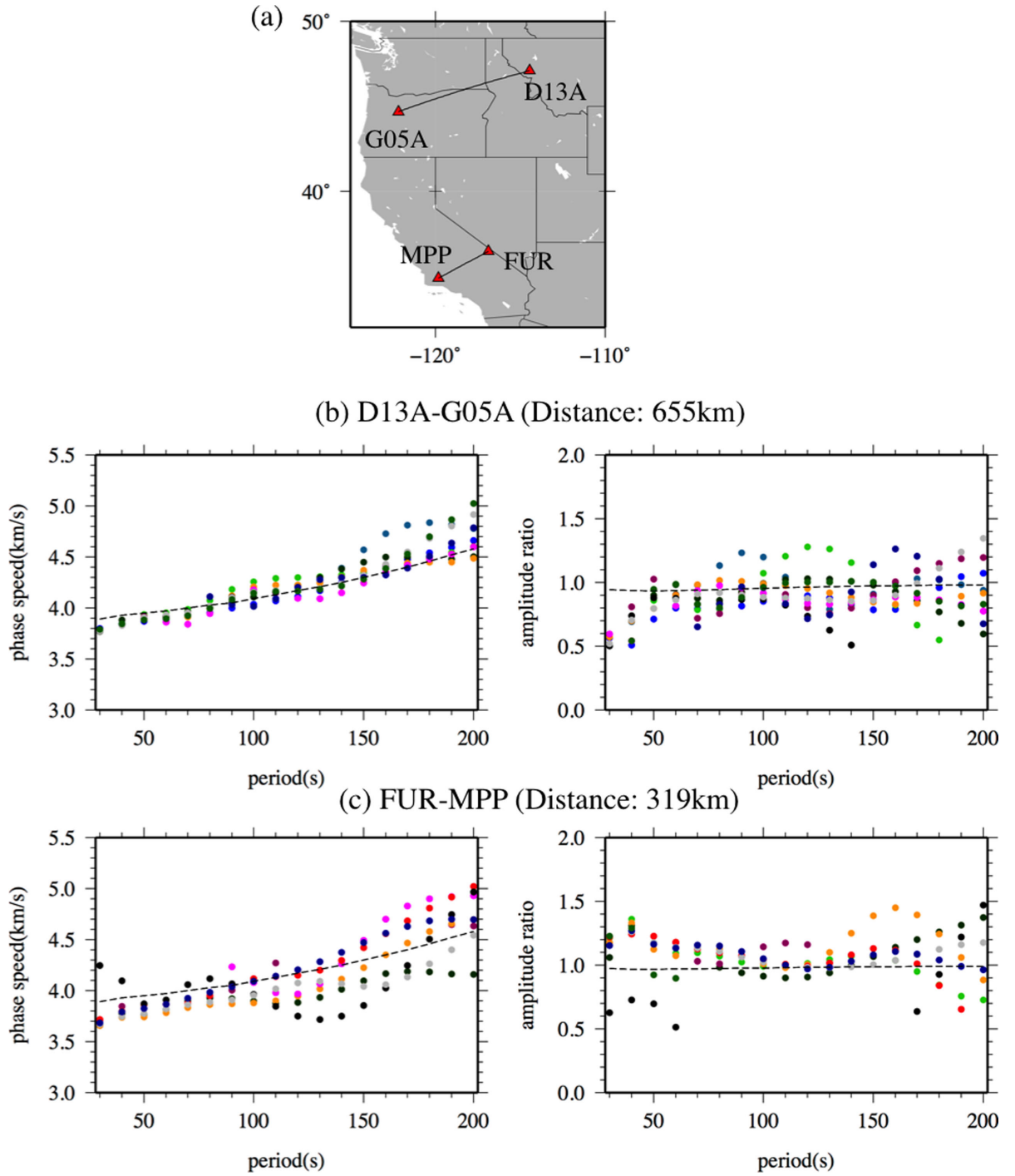

Figure 8. Examples of observed dispersion curves for Rayleigh-wave phase speeds and amplitude ratios. (a) Interstation paths between D13A and G05A, and between FUR and MPP stations. (b, c) Observed dispersion curves for the two interstation paths. Different colours of plots represent the measurements for different seismic sources (12 events for D13A-G05A, and 13 events for FUR-MPP), and dashed lines indicate the reference values calculated for PREM with a smoothed 220 km discontinuity.

& Wong (1986), the amplitude anomaly caused by focusing for a single station can be given as follows,

$$\ln A_F(\omega) = \frac{1}{2\sin\Delta}\int_0^{\Delta} \sin(\Delta-\phi)\left[\sin\phi\,\partial_\theta^2 - \cos\phi\,\partial_\phi\right]\frac{\delta c}{c_0}(\omega)\mathrm{d}\phi, \tag{20}$$

where Δ is the epicentral distance, ϕ the along-path coordinate, θ the path-perpendicular coordinate, and ∂_ϕ and ∂_θ the derivatives with respect to each coordinate. The corresponding amplitude anomaly for the case of interstation amplitude ratios can be derived from the differences for the two stations as follows,

$$\ln\left(\frac{A_F^{\mathrm{far}}}{A_F^{\mathrm{near}}}\right) = \frac{1}{2\sin(\Delta_n + d\Delta)}\int_0^{d\Delta} \sin(d\Delta-\phi')\left[\sin(\Delta_n+\phi')\partial_\theta^2 - \cos(\Delta_n+\phi')\partial_\phi\right]\frac{\delta c}{c_0}(\omega)\mathrm{d}\phi, \tag{21}$$

Downloaded from http://gji.oxfordjournals.org/ at Hokkaido University on October 20, 2015

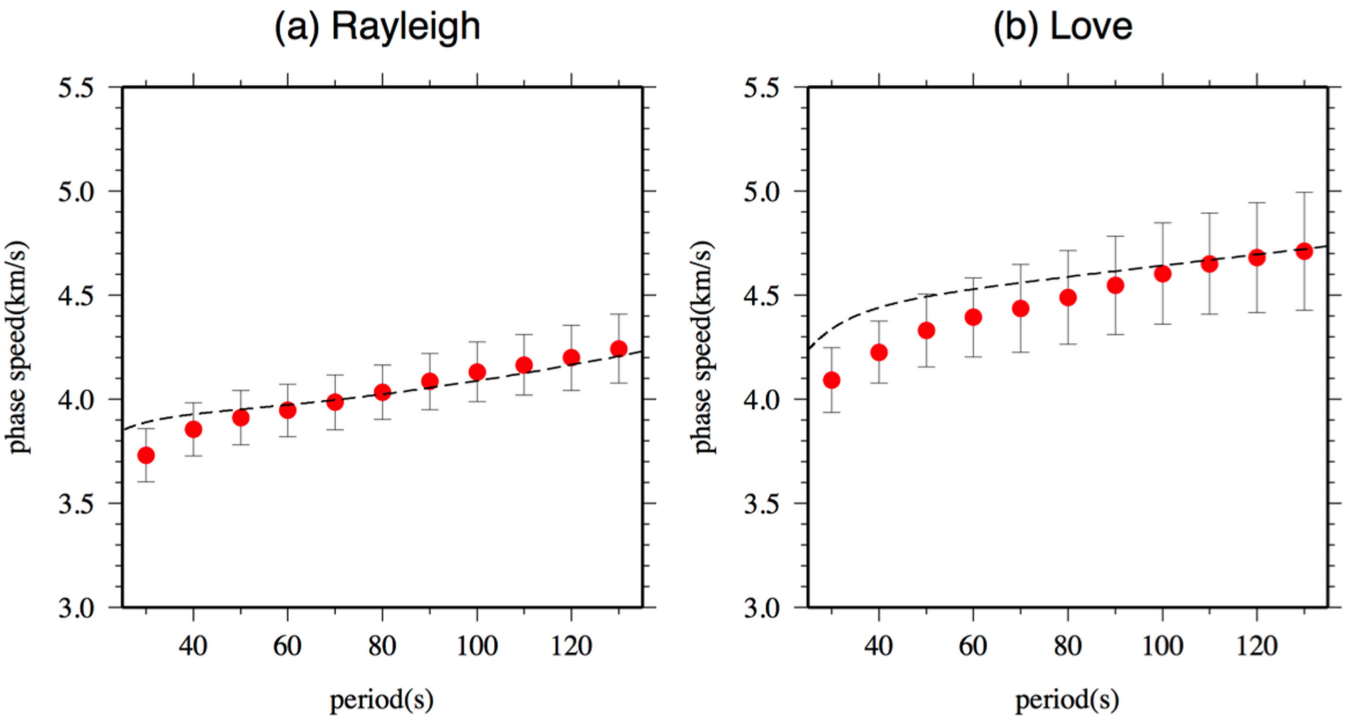

Figure 9. Average phase speeds (red dots) and standard errors for (a) Rayleigh waves and (b) Love waves calculated from our final data set used for phase speed mapping. Dashed lines indicate the dispersion curves for PREM.

where Δ_n is the epicentral distance of the nearer station, $d\Delta$ is the interstation distance and $\phi' = \phi - \Delta_n$. We approximate that $\Delta_n \sim \Delta_n + d\Delta$ on the assumption that $\Delta_n \gg d\Delta$.

The final term in eq. (19) represents the anelastic attenuation between the two stations. The majority of our interstation amplitude ratios are measured for short distances around 500 km, which encompasses only a couple of phase cycles of intermediate/long-period surface waves. The effects of lateral variations of anelastic attenuation on the amplitude anomaly for such short paths are comparable or much less than the measurement errors of amplitude ratios. Thus, in this study, we simply evaluate this attenuation factor using the reference Q_0 values of PREM as follows,

$$\ln \frac{A_Q^{\rm far}}{A_Q^{\rm near}} = -\frac{\omega d\Delta}{2U_0 Q_0}. \tag{22}$$

Eq. (19) can then be written as,

$$A'(\omega) = \ln A_R^{\rm far}(\omega) - \ln A_R^{\rm near}(\omega) + A'_F(\omega), \tag{23}$$

where $A' = \ln(A^{\rm far}/A^{\rm near}) - \ln(A_Q^{\rm far}/A_Q^{\rm near})$, which represents the observed amplitude ratio corrected with a reference attenuation (Note that the geometrical spreading and instrument responses are corrected beforehand). A' is used as input amplitude data for the joint inversion with phase data. $A'_F = \ln(A_F^{\rm far}/A_F^{\rm near})$ represents the amplitude anomaly caused by elastic focusing/defocusing due to the lateral variations of phase speeds as shown in eq. (21).

Using eqs (11) and (23), the measured interstation phase speed and amplitude ratios are inverted simultaneously for the receiver amplification term $\ln A_R$ (or the station correction term) for each station as well as phase speed distribution $\delta c/c_0$, which is expanded in the spherical B-spline functions as given in eq. (13).

We use the weighting scheme for equalizing different data sets of phase and amplitude, in the similar way to Julia *et al.* (2000),

$$E = \frac{p}{\sigma_c^2 N_c}\sum_{i=1}^{N_c} w_i^2 \left(s_i - \sum_{j=1}^{M} G_{ij} m_j\right)^2 + \frac{1-p}{\sigma_A^2 N_A}\sum_{i=1}^{N_A} w_i^2 \left(a_i - \sum_{j=1}^{M} F_{ij} m_j\right)^2, \tag{24}$$

where s_i and a_i are the observed phase speed perturbations and logarithm of amplitude ratios, N_c and N_A are the numbers of data for phase and amplitude data set, and p is the factor determining the relative weight given to the phase and amplitude data and varies from 0 to 1. F_{ij} represents eq. (21) with spherical spline functions. σ_c and σ_A are respectively the standard deviations of phase and amplitude ratios for each period (summarized in Tables 2 and 3), and w_i is the weight factor (or the reliability parameter in this study) for each measurement.

4.2 Phase speed maps of North America

Fig. 9 shows the average phase speeds of our data set, which tend to be slower than the reference phase speed estimated from PREM in the period range less than 60 s for Rayleigh waves and 110 s for Love waves. This reflects the effects of conspicuous slow anomalies of the crust and uppermost mantle in the western United States.

To evaluate the horizontal resolution of tomographic models, we perform checkerboard resolution tests with a variety of cell sizes. Some examples for Rayleigh-wave phase speed maps at 80 s using only phase data are displayed in Fig. 10, with cell sizes varying from 2 to 4°. The original checkerboard patterns include the maximum perturbations of ±4.8 per cent from the reference phase speed. In all cases, most areas of the western regions of North America are resolved well. On the other hand, the achievable resolution in the

Downloaded from http://gji.oxfordjournals.org/ at Hokkaido University on October 20, 2015

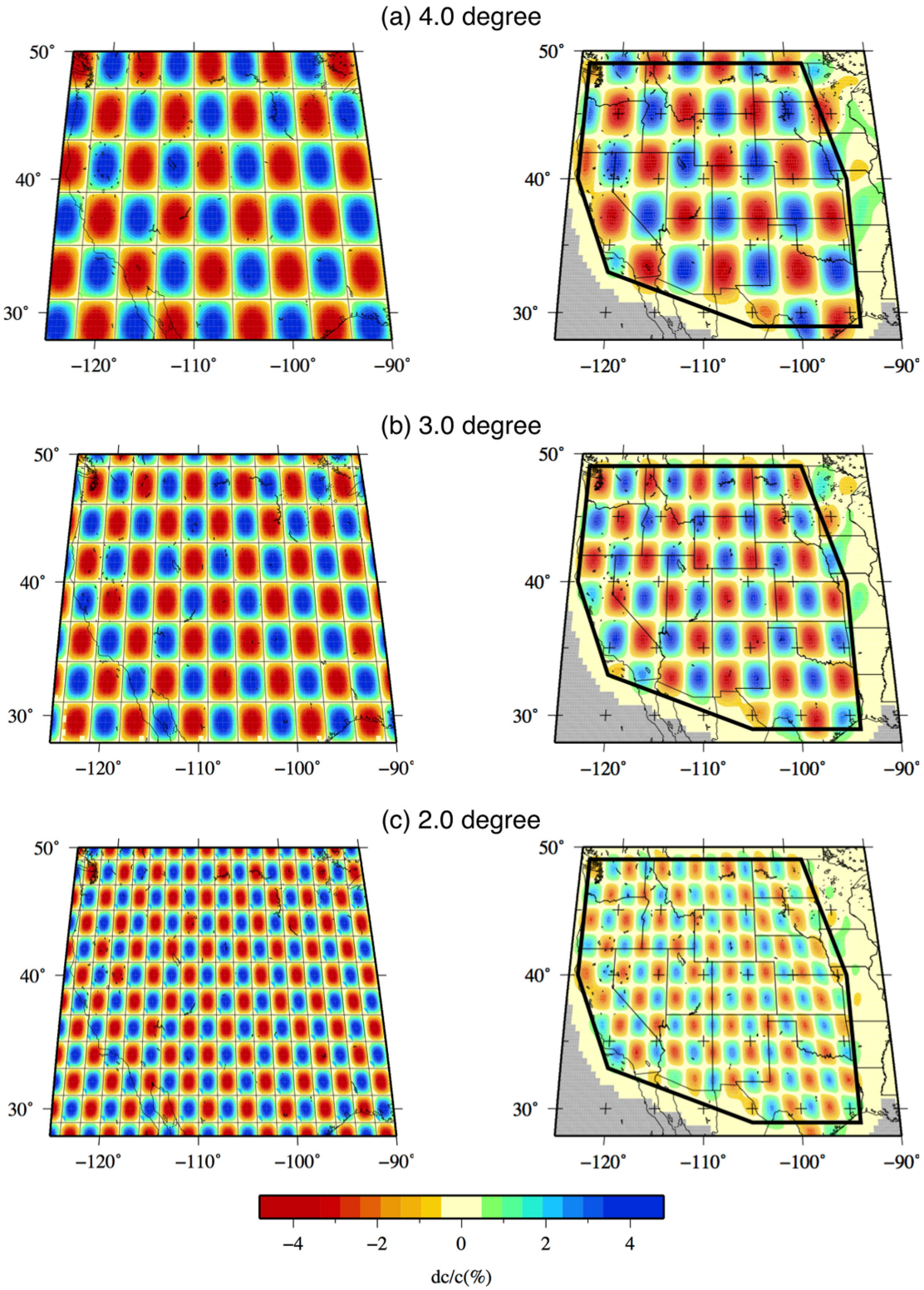

Figure 10. Examples of checkerboard resolution tests for Rayleigh-wave phase speed maps at 80 s with cell sizes of (a) 4.0°, (b) 3.0° and (c) 2.0°. Left panels are input checkerboard patterns, and right retrieved models. The black solid line represents the well-resolved areas with our data set.

eastern area from 95°W longitude tends to be limited due to the smaller numbers of crossing paths in the eastern margin of our target region.

The phase speed maps for the fundamental-mode Rayleigh and Love waves using phase data only are shown in Figs 11 and 12 in the period range between 30 and 130 s. These maps are plotted as perturbations from the average phase speed at each period shown in Fig. 9. The variance reductions achieved by inversions for phase speed maps with phase data, with respect to the average phase speeds of our measurements (Fig. 9), are about 18–60 per cent for Rayleigh

Downloaded from http://gji.oxfordjournals.org/ at Hokkaido University on October 20, 2015

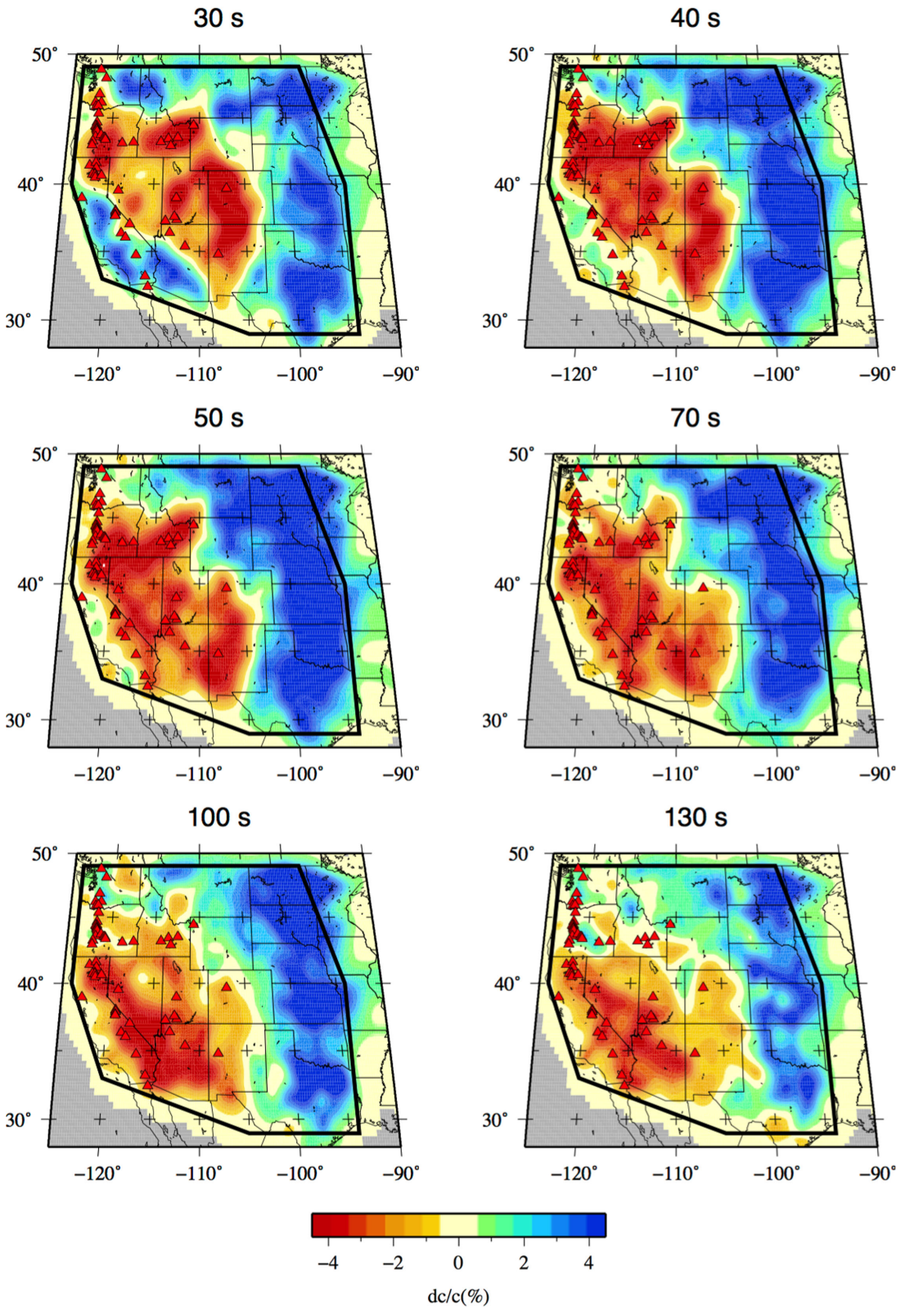

Figure 11. Rayleigh-wave phase speed maps derived from the phase data at periods from 30 to 130 s. Red triangles indicate the distribution of volcanoes taken from Siebert & Simkin (2002). The black solid line represents the well-resolved areas with our data set.

waves and 10–25 per cent for Love waves in the period range between 30 and 130 s. The variance reductions of our model tend to be lower than those of other phase speed models with the single-station analysis (e.g. Yoshizawa & Ekström 2010) or the two-station analysis based on single-station measurements (Foster *et al.* 2014b) in the same region. This implies the interference of non-plane waves and higher modes as well as off-great-circle propagation may have non-negligible influence on our interstation measurements based on

Downloaded from http://gji.oxfordjournals.org/ at Hokkaido University on October 20, 2015

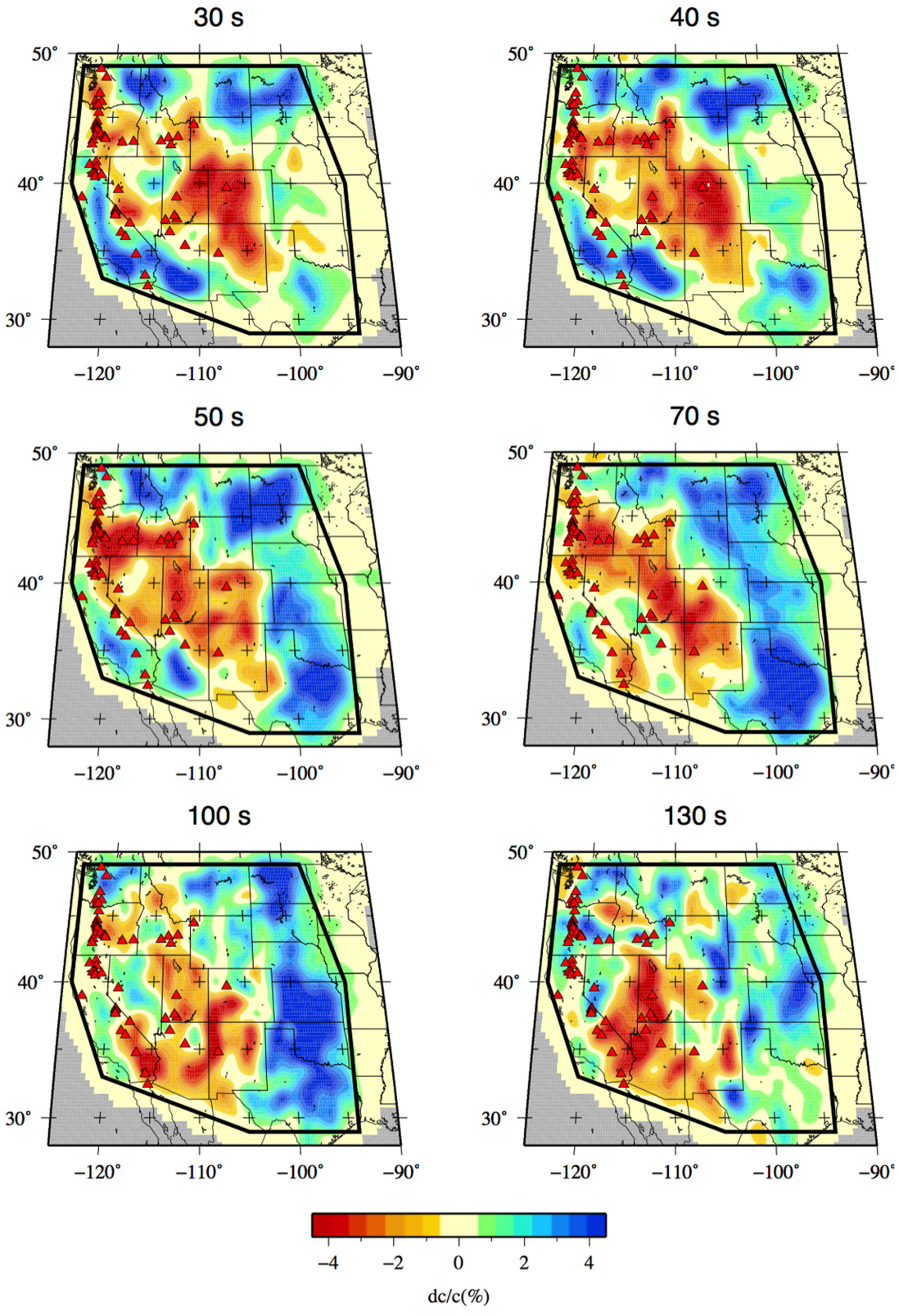

Figure 12. Same as Fig. 11, but for Love waves.

a direct waveform matching, resulting in large scatters in the dispersion measurements for the similar paths (e.g. Fig. 8). Nevertheless, the resultant models are consistent with the earlier North American models on a large scale.

Fig. 13 shows the results of checkerboard resolution tests for the phase speed maps derived from joint inversions of phase and amplitude data for the vertical-component Rayleigh waves. The results indicate that the patterns of checkerboards are apt to be smeared

Downloaded from http://gji.oxfordjournals.org/ at Hokkaido University on October 20, 2015

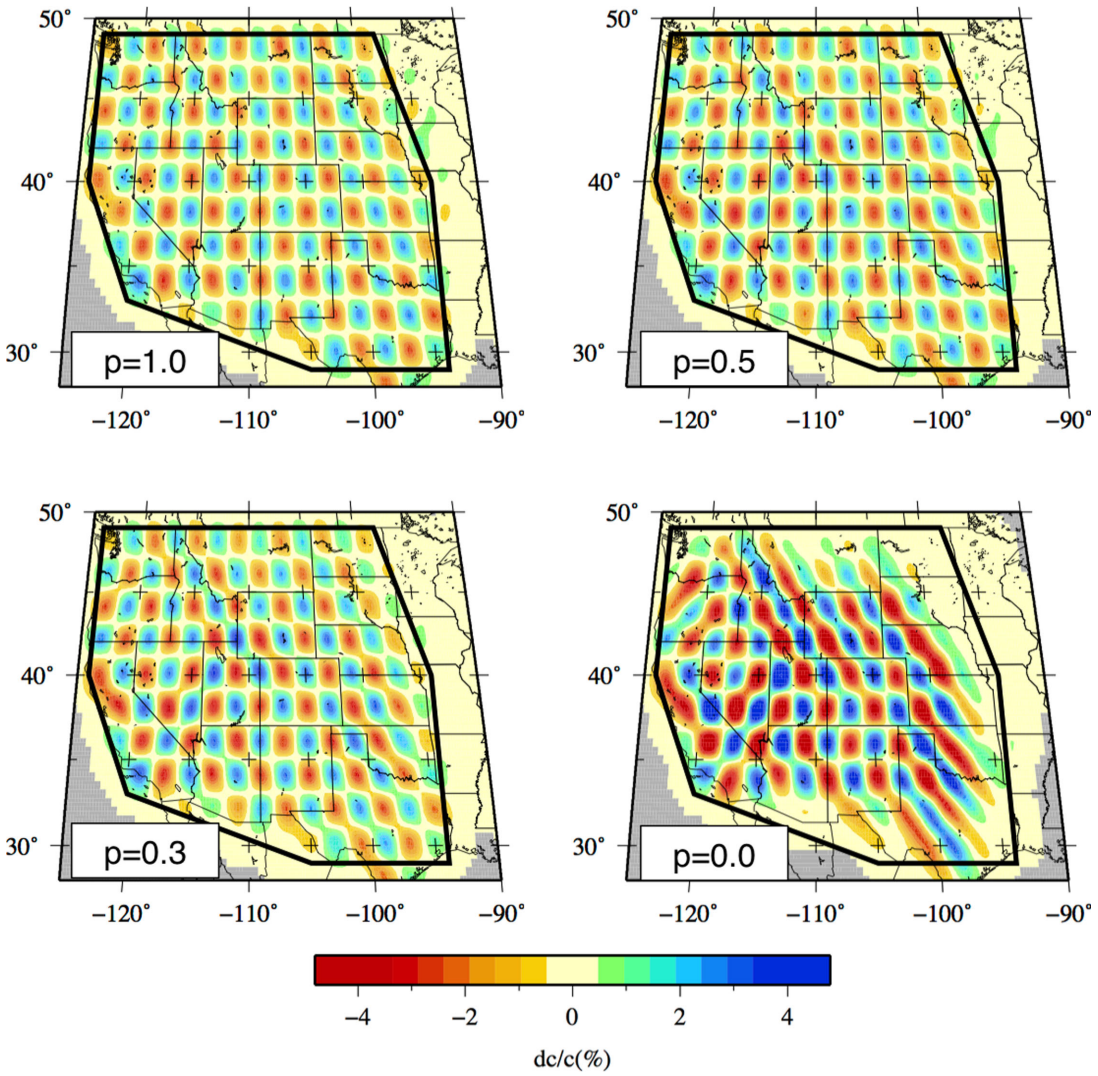

Figure 13. Checkerboard resolution tests with the joint inversion of phase and amplitude data for Rayleigh waves at 80 s, for a varying weight factor p on phase data.

to some extent as we weight more on the amplitude data because the number of paths for amplitude tends to be limited compared to phase data (see Table 2). However, the retrieved strength of velocity perturbation in the checkerboard models tend to be better as the weight on amplitude becomes larger (or, as p becomes smaller).

The average strengths of retrieved phase speed perturbations with respect to the input model, calculated in the area encompassed by the black line in Fig. 13, are 64 per cent for phase data only ($p = 1.0$), 68 per cent ($p = 0.5$), 70 per cent ($p = 0.3$), and 84 per cent for amplitude data only ($p = 0.0$). This represents the better resolving power of amplitude data for the second derivatives of velocity perturbation, resulting in the better recovery of the strength of velocity perturbation than phase data, although the achievable horizontal resolution may be lowered to some extent due to the limited numbers of amplitude measurements.

We display the phase speed maps obtained from the joint inversions of phase and amplitude data in Fig. 14(a) and the spatial variation of the station correction term in Fig. 14(c). The variance reduction for both amplitude and phase terms as a function of the data weight factor p is summarized in Fig. 14(b). In this study, we choose the map for $p = 0.3$ (giving more weight to the amplitude data) as the best compromised model derived from our phase and amplitude data.

In Fig. 15, we compare our phase speed maps with one of the latest results by Foster *et al.* (2014b), which is based on the interstation surface-wave phase speed data. Foster *et al.* (2014b) have re-extracted phase speed information between two stations by employing single-station measurements of surface-wave phase speed for USArray stations by Ekström (2011). Although we have used a different and independent approach to the interstation phase speed measurements from Foster *et al.*, large-scale heterogeneity patterns of our phase speed models, for both Rayleigh and Love waves, are highly consistent with those derived by Foster *et al.* (2014b). The correlations between the two models are 0.88–0.93 for Rayleigh waves and 0.67–0.77 for Love waves in the period range between 30 and 100 s. This implies and supports the validity and utility of our new measurement technique.

5 DISCUSSION

The western half of North America has been well investigated by seismic tomography at regional scale with a variety of

Downloaded from http://gji.oxfordjournals.org/ at Hokkaido University on October 20, 2015

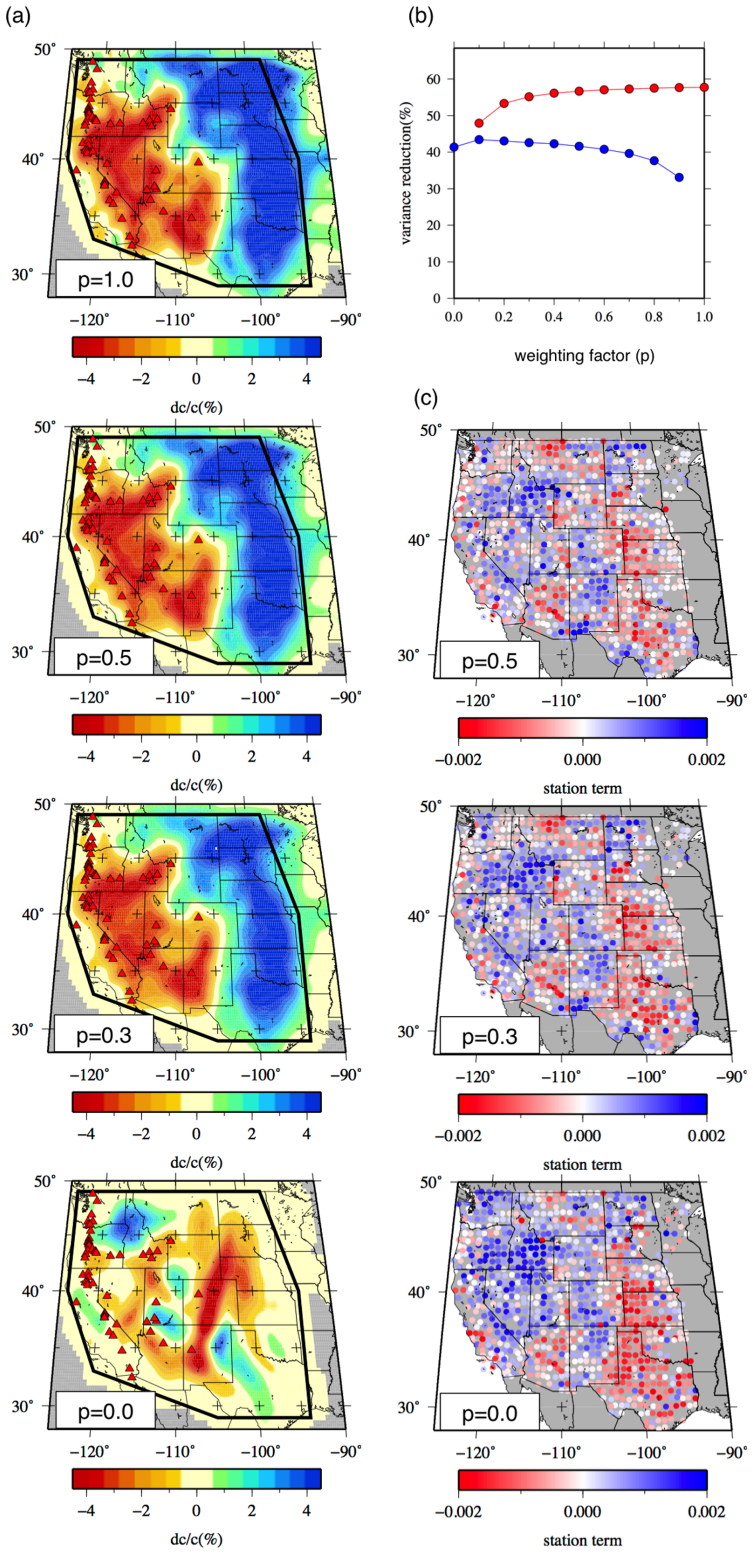

Figure 14. (a) Phase speed maps from the joint inversions of Rayleigh-wave phase and amplitude data at 60 s with a different data weight factor p which varies from 0 to 1. (b) Variance reductions of amplitude (blue) and phase (red) as a function of the data weight factor p. (c) Spatial distributions of the station-correction term.

techniques and data sets (e.g. Shapiro *et al.* 2005; Lin & Ritzwoller 2011; Obrebski *et al.* 2011). This area encompasses a variety of complex tectonic features, including regions with east–west extension, active volcanoes, the organic belt including Rocky Mountains and the stable cratonic region (Fig. 1). The Rocky Mountains divides the major tectonic features of the United States; the tectonically active western region including the subduction of the Juan de Fuca plate as well as the Yellowstone hotspot, and the eastern region with stable cratons (e.g. van der Lee & Nolet 1997).

Downloaded from http://gji.oxfordjournals.org/ at Hokkaido University on October 20, 2015

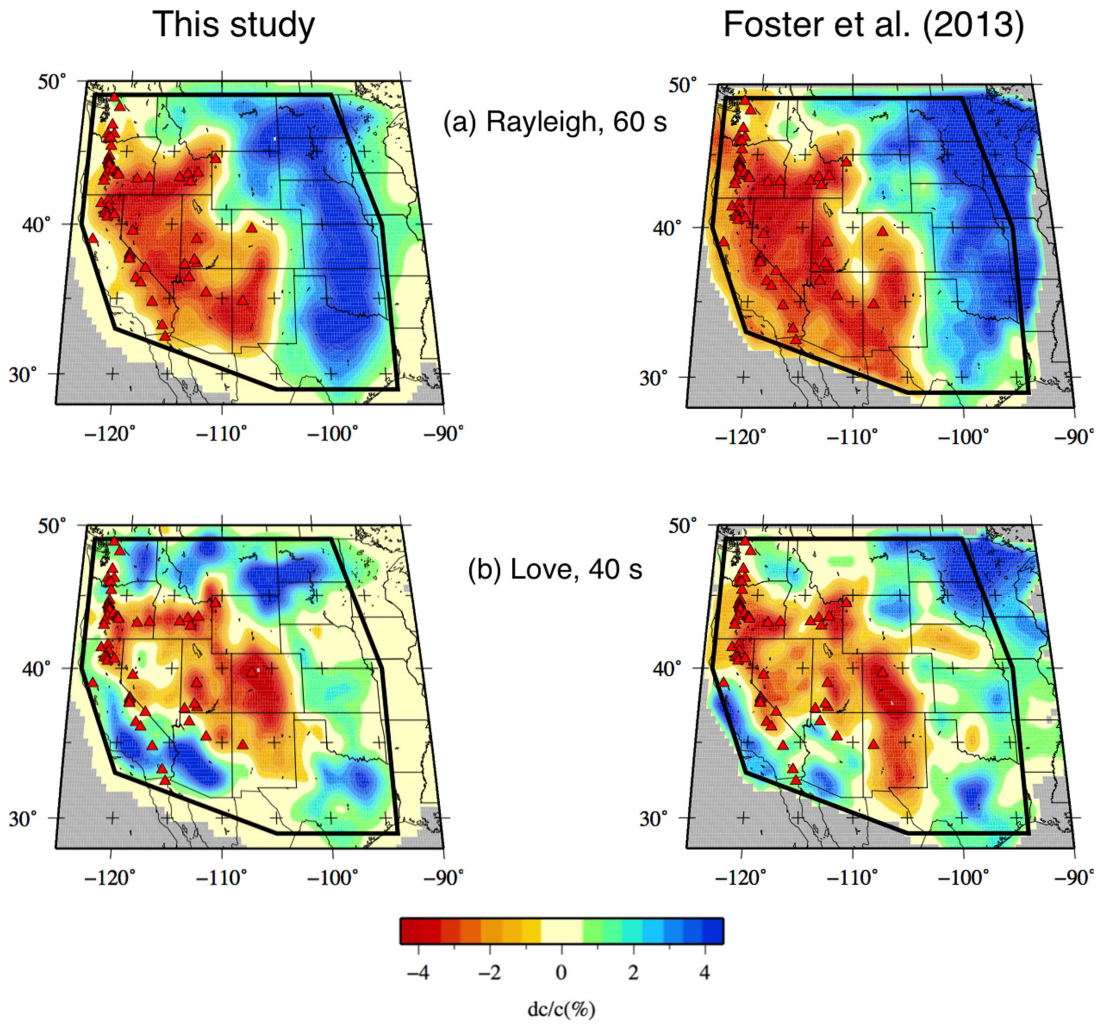

Figure 15. Comparisons between the phase speed models derived from (left) this study and (right) an earlier work by Foster *et al.* (2014b) for (a) Rayleigh waves at 60 s (joint inversion of phase and amplitude data) and (b) Love waves at 40 s (phase data only).

In the Rayleigh-wave phase speed maps (Fig. 11), a large-scale slow anomaly occupies the western United States, while fast anomalies are observed in the Great Plains in the central United States. We can find strong slow anomalies localized in the Snake River Plain, the eastern and western part of Basin and Range, and the Rio Grande Rift in the Rayleigh-wave phase speed maps at the periods between 30 and 70 s. A plume source beneath Yellowstone and the Snake River Plain has been found down to the depth of 200 km in recent V_P and V_S structures (Waite *et al.* 2006), which is also consistent with our observation. In the Basin and Range province, seismic activities dominated by normal faulting are concentrated along its eastern and western boundaries (Pancha *et al.* 2006), which suggests that large extensional strains have deformed this region. The Rio Grande Rift has also undergone lithospheric extension during the middle to late Cenozoic deformation (e.g. Baldridge *et al.* 1991). The slow anomalies in this region can be interpreted as high heat flow in the crust and uppermost mantle (e.g. Goes & Lee 2002).

In the period range between 30 and 70 s of Rayleigh-wave models, Colorado Plateau can be identified as a slightly faster region than the surrounding areas at around 37°N and 110°W. This feature tends to be clearer in the phase speed models from the joint inversion of phase and amplitude data (Fig. 14), in which the local velocity gradient can be better constrained. A recent tomographic study of body waves in this region (Sine *et al.* 2008) have shown that Paleozoic mantle lithosphere reaches down to the depth of 100 km or deeper beneath the Colorado Plateau, which is well reflected in our Rayleigh-wave models that show relatively faster anomalies in this area than its surroundings.

A fast phase speed anomaly is seen in the southwestern coast including Great Valley and Sierra Nevada, particularly at 30 s for Rayleigh waves and 30–50 s for Love waves, whereas slow anomalies dominate this area in the longer period range. Godfrey *et al.* (1997) have studied the complex structure and tectonic history of this region and indicated that the Great Valley basement is oceanic crust underlain by oceanic mantle, which is vertically stacked above continental crust and mantle.

The general features of Love-wave models also indicate the slow anomalies in the Snake River Plains, the Cascade range, the eastern margin of Basin and Range, and the Rio Grande Rift. The quality of our measurements for Love waves tends to be lower than that for Rayleigh waves, probably due to larger noises and errors in the horizontal components. Although we have assumed that a plane wave propagates along great-circle path in the process of waveform fitting, this assumption may be too simplistic to treat the horizontal components, which tends to be more sensitive to the deviations of arrival angles from the great circle. To improve the quality of phase

Downloaded from http://gji.oxfordjournals.org/ at Hokkaido University on October 20, 2015

speed models of Love waves, a more rigorous way to correct the arrival angles of incoming plane waves with an array analysis may be of help (e.g. Foster *et al.* 2014b).

The results of the joint inversion of phase and amplitude data, with the varying weight factor p, are displayed in Figs 13 and 14(a). The phase speed map derived from phase data only (i.e. $p = 1.0$) reflects large-scale tectonic features including the strong contrast between fast anomaly in the east and slower anomaly in the west. As we apply more weight on the amplitude data (i.e. decreasing p), local-scale features, which are characterized by larger velocity gradients, tend to be identified clearly; for example, significant slow anomalies in Yellow Stone, Snake River Plains and Rio Grande Rift. These results are in good agreement with the other independent observations, such as the arrival-angle deviations of surface waves (Foster *et al.* 2014a) which have a significant influence on the observed amplitude anomalies. The spatial distribution of station correction term in Fig. 14(c) represents local amplification term of observed amplitude, which shows a clear correlation with the velocity structure and is also very similar to the local amplification of surface waves by Lin *et al.* (2012).

Our results indicate that interstation amplitude data measured using a dense array can be useful to reconstruct shorter-wavelength elastic structures, owing to its sensitivities to the second derivatives of phase speeds across the path. In this analysis, we fixed the anelastic attenuation terms due to the intrinsic difficulty in separating the spatial variations of anelastic attenuation from observed amplitudes for short paths around 500 km in the frequency range used in this study. To construct attenuation models, single-station amplitude measurements for longer paths may be preferable (e.g. Dalton & Ekström 2006). We expect that the phase speed models derived from the joint inversion of phase and amplitude data in this study, which exhibit a better recovery in velocity perturbation, can be of help in correcting the effects of focusing/defocusing included in the observed amplitude and eventually constraining an attenuation model on regional scale in combination with single-station measurements.

6 CONCLUSIONS

We have developed a new method for measuring interstation phase speed and amplitude ratio based on the fully nonlinear waveform fitting technique, which allows us to collect a large number of phase and amplitude measurements for short interstation paths (less than 1000 km) using a dense broad-band seismic array in the United States. The reliability parameter introduced for quantifying the waveform fit allows us to select the reliable dispersion measurements in an automated manner. This method has been applied to the transportable array of USArray, and we have collected the large numbers of phase speed dispersion data for the fundamental Rayleigh and Love waves in the period range between 30 and 130 s, which are then inverted for phase speed maps. The major features of the phase speed maps are consistent with earlier tomographic studies, indicating the validity of our new measurement technique for phase speeds of surface waves.

With the new interstation measurement method in combination with the high-density broad-band seismic array, we could gather a large number of short paths with typical interstation distances of about 300–800 km, which are much shorter than the average path length of the conventional single-station analysis which is normally over 2000 km. The bundle of shorter paths of this study allows us to improve the achievable horizontal resolution of phase speed models to be about 150–200 km, which is nearly a half of those achieved by the typical surface wave models with single station analysis.

Not only the interstation phase speed data but also the interstation amplitude ratio data are used to constrain the phase speed model in this study. The results of joint inversion of phase and amplitude data clearly suggest that the measured amplitude through the nonlinear waveform fitting can be used to constrain the velocity structure, with a better recovery of the velocity perturbations of smaller-scale local heterogeneities in tomographic models, as has been suggested in earlier work (e.g. Laske & Masters 1996).

Our joint inversions of phase and amplitude data are based on a simple assumption of the plane wave propagation of surface waves along the great-circle paths, though the effects of non-plane wave propagation can be significant for a shorter period range than 50 s (e.g. Friederich *et al.* 1994), which may result in the biases in the measured phase speeds (Wielandt 1993). Alternative approaches such as the multistation analysis for arrival-angle estimation (e.g. Foster *et al.* 2014b) and/or two-plane wave analysis (e.g. Forsyth & Li 2005) may be of help to remedy such effects caused by non-plane waves in laterally heterogeneous media.

Our new method of interstation waveform fitting technique based on the transfer function is simple, but can be useful for extracting a large number of the structural information for short paths that are almost comparable to the scale of wavelength of surface waves, which cannot readily be extracted from the widely used single-station measurements. Such short path information of both phase speed and amplitude ratios can be of great help in high-resolution mapping of the upper-mantle structure, in conjunction with the growing numbers of high-density broad-band arrays in many regions in the world.

ACKNOWLEDGEMENTS

We thank the IRIS Data Management Center for the provision of seismic waveform data, particularly the networks TA and CI used in this study. We also thank Malcolm Sambridge for the provision of the Neighbourhood Algorithm code. Many constructive and critical comments by anonymous reviewers and the editor Gabi Laske were helpful for improving the manuscript. This study was partly supported by Grant-in-Aid for Scientific Research (Nos. 22654053, 24740298 and 26400443) to KY from the Ministry of Education, Culture, Sports, Science and Technology of Japan.

REFERENCES

Bakirci, T., Yoshizawa, K. & Özer, M.F., 2012. Three-dimensional S-wave structure of the upper mantle beneath Turkey from surface wave tomography, *Geophys. J. Int.,* **190**(2), 1058–1076.

Baldridge, W. *et al.*, 1991. Middle to late cenozoic magmatism of the southeastern Colorado plateau and central Rio Grande rift (New Mexico and Arizona, U.S.A.): a model for continental rifting, *Tectonophysics,* **197** (2-4), 327–354.

Baumont, D., Paul, A., Zandt, G., Beck, S.L. & Pedersen, H.A., 2002. Lithospheric structure of the central Andes based on surface wave dispersion, *J. geophys. Res.,* **107**(B12), 2371, doi:10.1029/2001JB000345.

Bird, P., 2003. An updated digital model of plate boundaries, *Geochem. Geophys. Geosyst.,* **4**(3), 1027, doi:10.1029/2001GC000252.

Boschi, L., Becker, T.W., Soldati, G. & Dziewonski, A.M., 2006. On the relevance of Born theory in global seismic tomography, *Geophys. Res. Lett.,* **33**(6), L06302, doi:10.1029/2005GL025063.

Burdick, S. *et al.*, 2010. Model upgrade January 2010: upper mantle heterogeneity beneath North America from traveltime tomography with global and USArray transportable array data, *Seismol. Res. Lett.,* **81**(5), 689–693.

Downloaded from http://gji.oxfordjournals.org/ at Hokkaido University on October 20, 2015

Dalton, C.A. & Ekström, G., 2006. Global models of surface wave attenuation, *J. geophys. Res.,* **111**(B5), 1–19.

Darbyshire, F.A. & Lebedev, S., 2009. Rayleigh wave phase-velocity heterogeneity and multilayered azimuthal anisotropy of the Superior Craton, Ontario, *Geophys. J. Int.,* **176**(1), 215–234.

Debayle, E. & Kennett, B.L.N., 2000. The Australian continental upper mantle: structure and deformation inferred from surface waves, *J. geophys. Res.,* **105**(B11), 25 423–25 450.

Debayle, E. & Ricard, Y., 2012. A global shear velocity model of the upper mantle from fundamental and higher Rayleigh mode measurements, *J. geophys. Res,* **117**(B10), B10308, doi:10.1029/2012JB009288.

Deschamps, F., Lebedev, S., Meier, T. & Trampert, J., 2008. Stratified seismic anisotropy reveals past and present deformation beneath the East-central United States, *Earth planet. Sci. Lett.,* **274**(3-4), 489–498.

Dziewonski, A.M. & Hales, A., 1972. Numerical Analysis of Dispersed Seismic Waves, *Bull. seism. Soc. Am.,* **47,** 39–84.

Dziewonski, A.M. & Anderson, D.L., 1981. Preliminary reference Earth model, *Phys. Earth planet. Inter.,* **25**(4), 297–356.

Ekström, G., 2011. A global model of Love and Rayleigh surface wave dispersion and anisotropy, 25-250 s, *Geophys. J. Int.,* **187**(3), 1668–1686.

Ekström, G., Tromp, J. & Larson, E., 1997. Measurements and global models of surface wave propagation, *J. geophys. Res.,* **102**(B4), 8137–8157.

Ekström, G., Dziewonski, A.M., Maternovskaya, N. & Nettles, M., 2005. Global seismicity of 2003: centroid-moment-tensor solutions for 1087 earthquakes, *Phys. Earth planet. Inter.,* **148**(2-4), 327–351.

Ekström, G., Abers, G.A. & Webb, S.C., 2009. Determination of surface-wave phase velocities across USArray from noise and Aki's spectral formulation, *Geophys. Res. Lett.,* **36**(18), L18301, doi:10.1029/2009GL039131.

Forsyth, D.W. & Li, A., 2005. Array Analysis of Two-Dimensional Variations in Surface Wave Phase Velocity and Azimuthal Anisotropy in the Presence of Multipathing Interference, in *Seism. Earth Array Anal. Broadband Seism. Geophys. Monogr. Ser.,* Vol. **157,** pp. 81–97, eds. Levander, A. & Nolet, G., AGU.

Foster, A., Ekström, G. & Hjörleifsdóttir, V., 2014a. Arrival-angle anomalies across the USArray Transportable Array, *Earth planet. Sci. Lett.,* **402,** 58–68.

Foster, A., Ekstrom, G. & Nettles, M., 2014b. Surface wave phase velocities of the Western United States from a two-station method, *Geophys. J. Int.,* **196**(2), 1189–1206.

Friederich, W., Wielandt, E. & Stange, S., 1994. Non-plane geometries of seismic surface wavefields and their implications for regional surface-wave tomography, *Geophys. J. Int.,* **119**(3), 931–948.

Godey, S., Snieder, R., Villase, A. & Benz, H.M., 2003. Surface wave tomography of North America and the Caribbean using global and regional broad-band networks: phase velocity maps and limitations of ray theory, *Geophys. J. Int.,* **152,** 620–632.

Godfrey, N.J., Beaudoin, B.C. & Klemperer, S.L., 1997. Ophiolitic basement to the Great Valley forearc basin, California, from seismic and gravity data: implications for crustal growth at the North American continental margin, *Bull. geol. Soc. Am.,* **109**(12), 1536–1562.

Goes, S. & Lee, S.V.D., 2002. Thermal structure of the North American uppermost mantle inferred from seismic tomography, *J. geophys. Res.,* **107**(B3), B32050, doi:10.1029/2000JB000049.

Isse, T., Suetsugu, D., Shiobara, H., Sugioka, H., Yoshizawa, K., Kanazawa, T. & Fukao, Y., 2006a. Shear wave speed structure beneath the South Pacific superswell using broadband data from ocean floor and islands, *Geophys. Res. Lett.,* **33**(16), L16303, doi:10.1029/2006GL026872.

Isse, T. *et al.*, 2006b. Three-dimensional shear wave structure beneath the Philippine Sea from land and ocean bottom broadband seismograms, *J. geophys. Res.,* **111**(B6), B06310, doi:10.1029/2005JB003750.

Julia, J., Ammon, C.J., Herrmann, R.B. & Correig, A.M., 2000. Joint inversion of receiver function and surface wave dispersion observations, *Geophys. J. Int.,* **143,** 99–112.

Kaviani, A., Paul, A., Bourova, E., Hatzfeld, D., Pedersen, H. & Mokhtari, M., 2007. A strong seismic velocity contrast in the shallow mantle across the Zagros collision zone (Iran), *Geophys. J. Int.,* **171**(1), 399–410.

Larson, E. & Ekström, G., 2001. Global models of surface wave group velocity, *Pure appl. Geophys.,* **158,** 1377–1399.

Laske, G. & Masters, G., 1996. Constraints on global phase velocity maps from long-period polarization data, *J. geophys. Res.,* **101**(B7), 16 059–16 075.

Lebedev, S. & Nolet, G., 2003. Upper mantle beneath Southeast Asia from S velocity tomography, *J. geophys. Res.,* **108**(B1), 2048, doi:10.1029/2000JB000073.

Lebedev, S. & van der Hilst, R.D., 2008. Global upper-mantle tomography with the automated multimode inversion of surface and S-wave forms, *Geophys. J. Int.,* **173**(2), 505–518.

Li, A., Forsyth, D.W. & Fischer, K.M., 2003. Shear velocity structure and azimuthal anisotropy beneath eastern North America from Rayleigh wave inversion, *J. geophys. Res.,* **108**(B8), 2362, doi:10.1029/2002JB002259.

Lin, F.-C. & Ritzwoller, M.H., 2011. Helmholtz surface wave tomography for isotropic and azimuthally anisotropic structure, *Geophys. J. Int.,* **186**(3), 1104–1120.

Lin, F.-C., Ritzwoller, M.H. & Snieder, R., 2009. Eikonal tomography: surface wave tomography by phase front tracking across a regional broad-band seismic array, *Geophys. J. Int.,* **177**(3), 1091–1110.

Lin, F.-C., Tsai, V.C. & Ritzwoller, M.H., 2012. The local amplification of surface waves: a new observable to constrain elastic velocities, density, and anelastic attenuation, *J. geophys. Res.,* **117**(B6), B06302, doi:10.1029/2012JB009208.

Marone, F., Gung, Y. & Romanowicz, B., 2007. Three-dimensional radial anisotropic structure of the North American upper mantle from inversion of surface waveform data, *Geophys. J. Int.,* **171**(1), 206–222.

Montagner, J.-P. & Tanimoto, T., 1991. Global upper mantle tomography of seismic velocities and anisotropies, *J. geophys. Res.,* **96**(B12), 20 337–20 351.

Nettles, M. & Dziewonski, A.M., 2008. Radially anisotropic shear velocity structure of the upper mantle globally and beneath North America, *J. geophys. Res.,* **113**(B2), B02303, doi:10.1029/2006JB004819.

Obrebski, M., Allen, R.M., Pollitz, F. & Hung, S.-H., 2011. Lithosphere-asthenosphere interaction beneath the western United States from the joint inversion of body-wave traveltimes and surface-wave phase velocities, *Geophys. J. Int.,* **185**(2), 1003–1021.

Paige, C.C. & Saunders, M.A., 1982. LSQR: an algorithm for sparse linear equations and sparse least squares, *ACM Trans. Math. Softw.,* **8**(1), 43–71.

Pancha, A., Anderson, J.G. & Kreemer, C., 2006. Comparison of seismic and geodetic scalar moment rates across the Basin and Range province, *Bull. seism. Soc. Am.,* **96**(1), 11–32.

Pedersen, H.A., 2006. Impacts of non-plane waves on two-station measurements of phase velocities, *Geophys. J. Int.,* **165**(1), 279–287.

Sambridge, M., 1999. Geophysical inversion with a neighbourhood algorithm-I. Searching a parameter space, *Geophys. J. Int.,* **138**(2), 479–494.

Shapiro, N.M., Campillo, M., Stehly, L. & Ritzwoller, M.H., 2005. High-resolution surface-wave tomography from ambient seismic noise, *Science,* **307**(5715), 1615–1618.

Siebert, L. & Simkin, T., 2002. *Volcanoes of the World: an Illustrated Catalog of Holocene Volcanoes and their Eruptions. Smithsonian Institution, Global Volcanism Program Digital Information Series, GVP-3*. Available at: http://www.volcano.si.edu.

Sine, C.R., Wilson, D., Gao, W., Grand, S.P., Aster, R., Ni, J. & Baldridge, W.S., 2008. Mantle structure beneath the western edge of the Colorado Plateau, *Geophys. Res. Lett.,* **35**(10), L10303, doi:10.1029/2008GL033391.

Trampert, J. & Woodhouse, J.H., 1995. Global phase velocity maps of Love and Rayleigh waves between 40 and 150 seconds, *Geophys. J. Int.,* **122**(2), 675–690.

van der Lee, S. & Nolet, G., 1997. Seismic image of the subducted trailing fragments of the Farallon plate, *J. geophys. Res.,* **102,** 22 815–22 838.

Downloaded from http://gji.oxfordjournals.org/ at Hokkaido University on October 20, 2015

van Heijst, H.J. & Woodhouse, J., 1997. Measuring surface-wave overtone phase velocities using a mode-branch stripping technique, *Geophys. J. Int.,* **131**(2), 209–230.

Visser, K., Trampert, J. & Kennett, B.L.N., 2008. Global anisotropic phase velocity maps for higher mode Love and Rayleigh waves, *Geophys. J. Int.,* **172**(3), 1016–1032.

Waite, G.P., Smith, R.B. & Allen, R.M., 2006. VP and VS structure of the Yellowstone hot spot from teleseismic tomography: evidence for an upper mantle plume, *J. geophys. Res.,* **111**(B4), B04303, doi:10.1029/2005JB003867.

Wielandt, E., 1993. Propagation and structural interpretation of non-plane waves, *Geophys. J. Int.,* **113,** 45–53.

Woodhouse, J.H. & Wong, Y.K., 1986. Amplitude, phase and path anomalies of mantle waves, *Geophys. J. Int.,* **87,** 753–773.

Yang, X., Taylor, S.R. & Patton, H.J., 2004. The 20-s Rayleigh wave attenuation tomography for central and southeastern Asia, *J. geophys. Res.,* **109**(B12), B12304, doi:10.1029/2004JB003193.

Yang, Y. & Forsyth, D.W., 2006. Regional tomographic inversion of the amplitude and phase of Rayleigh waves with 2-D sensitivity kernels, *Geophys. J. Int.,* **166**(3), 1148–1160.

Yoshizawa, K., 2014. Radially anisotropic 3-D shear wave structure of the Australian lithosphere and asthenosphere from multi-mode surface waves, *Phys. Earth planet. Inter.,* **235,** 33–48.

Yoshizawa, K. & Ekström, G., 2010. Automated multimode phase speed measurements for high-resolution regional-scale tomography: application to North America, *Geophys. J. Int.,* **183**(3), 1538–1558.

Yoshizawa, K. & Kennett, B., 2004. Multimode surface wave tomography for the Australian region using a three-stage approach incorporating finite frequency effects, *J. geophys. Res.,* **109**(B2), B02310, doi:10.1029/2002JB002254.

Yoshizawa, K. & Kennett, B.L.N., 2002. Non-linear waveform inversion for surface waves with a neighbourhood algorithm application to multimode dispersion measurements, *Geophys. J. Int.,* **149,** 118–133.

Yoshizawa, K., Yomogida, K. & Tsuboi, S., 1999. Resolving power of surface wave polarization data for higher-order heterogeneities, *Geophys. J. Int.,* **138**(1), 205–220.

Yoshizawa, K., Miyake, K. & Yomogida, K., 2010. 3D upper mantle structure beneath Japan and its surrounding region from inter-station dispersion measurements of surface waves, *Phys. Earth planet. Inter.,* **183**(1–2), 4–19.

Downloaded from http://gji.oxfordjournals.org/ at Hokkaido University on October 20, 2015